

# **Growth of Highly Conductive PtSe<sub>2</sub> Films Controlled by Raman Metrics for High-Frequency Photodetectors and Optoelectronic Mixers at 1.55 $\mu\text{m}$**

*Eva Desgué\*, Ivan Verschueren, Marin Tharrault, Djordje Dosenovic, Ludovic Largeau, Eva Grimaldi, Delphine Pommier, Doriane Jussey, Bérangère Moreau, Dominique Carisetti, Laurent Gangloff, Patrick Plouhinec, Naomie Messudom, Zineb Bouyid, Didier Pribat, Julien Chaste, Abdelkarim Ouerghi, Bernard Plaçais, Emmanuel Baudin, Hanako Okuno, Pierre Legagneux\**

E. Desgué, I. Verschueren, E. Grimaldi, D. Pommier, D. Jussey, D. Carisetti, L. Gangloff, P. Plouhinec, N. Messudom, Z. Bouyid, P. Legagneux  
Thales Research & Technology (TRT), 1 avenue Augustin Fresnel, 91120 Palaiseau, France  
E-mail: [eva.desgue@thalesgroup.com](mailto:eva.desgue@thalesgroup.com) and [pierre.legagneux@thalesgroup.com](mailto:pierre.legagneux@thalesgroup.com)

M. Tharrault, B. Plaçais, E. Baudin  
Laboratoire de Physique de l'École Normale Supérieure (LPENS), 24 Rue Lhomond, 75005 Paris, France

D. Dosenovic, B. Moreau, H. Okuno  
CEA Grenoble, 17 avenue des Martyrs, 38000 Grenoble, France

L. Largeau, J. Chaste, A. Ouerghi  
Center for Nanoscience and Nanotechnology (C2N), 10 boulevard Thomas Gobert, 91120 Palaiseau, France

D. Pribat  
Laboratoire de Physique des Interfaces et Couches Minces (LPICM), Ecole Polytechnique, 91120 Palaiseau, France

Keywords: 2D materials, transition metal dichalcogenides, platinum diselenide, Molecular Beam Epitaxy, Raman spectroscopy, optoelectronic mixing, infrared photodetection

Two-dimensional PtSe<sub>2</sub> exhibits outstanding intrinsic properties such as high carrier mobility, tunable bandgap, broadband absorption and air stability, making it ideal for (opto)electronic applications. However, achieving high crystalline quality films with controlled properties on low cost and insulating substrates remains challenging. Here, highly crystalline semimetallic PtSe<sub>2</sub> films are grown by molecular beam epitaxy on sapphire substrates. It is shown that a post-growth annealing remarkably improves the out-of-plane crystallinity of multilayer films and leads to the record film conductivity of 1.6 mS. In-depth structural analyses reveal the strong influence of the domain arrangement within the film on its electrical conductivity. Moreover, it is demonstrated that the commonly used E<sub>g</sub> Raman peak width, but also the A<sub>1g</sub> peak width, are both effective metrics for evaluating the quality of PtSe<sub>2</sub>: films with thinner E<sub>g</sub> and A<sub>1g</sub> peaks exhibit higher in-plane and out-of-plane crystalline quality, as well as higher conductivity. Finally, coplanar waveguides integrating a semimetallic PtSe<sub>2</sub> channel are fabricated on a 2-inch sapphire substrate to demonstrate optoelectronic devices operating at the 1.55 μm telecom wavelength: photodetectors with a record bandwidth of 60 GHz and the first PtSe<sub>2</sub>-based optoelectronic mixer with a 30 GHz bandwidth.

## 1. Introduction

Transition metal dichalcogenides (TMDs) are very promising two-dimensional (2D) materials for (opto)electronic applications<sup>[1,2,3,4]</sup> due to their thickness-dependent electronic properties, their various bandgap values ranging from the visible to the near-IR region, the strong light-matter interaction per 2D layer and also because they can be transferred and integrated onto CMOS or photonic platforms.<sup>[5,6,7]</sup> Platinum diselenide (PtSe<sub>2</sub>) is an original and remarkable TMD which can change its electronic nature as a function of the thickness: it is semiconducting for a few layers and becomes semimetallic for thicker ones. It also stands out because it can absorb in the IR, presents one of the highest theoretically predicted carrier mobility ( $> 4000 \text{ cm}^2 \cdot (\text{V} \cdot \text{s})^{-1}$ )<sup>[8]</sup> with experimental values above  $200 \text{ cm}^2 \cdot (\text{V} \cdot \text{s})^{-1}$  at room temperature and an excellent air stability.<sup>[9,10,11,12,13]</sup> Therefore, PtSe<sub>2</sub> is particularly suitable for optoelectronics in the IR domain.<sup>[14,15,16,17]</sup>

PtSe<sub>2</sub> has been widely studied for the fabrication of high-frequency ( $> 1 \text{ GHz}$ ) photodetectors operating at the telecom wavelength of 1.55 μm.<sup>[14,18,19,20]</sup> Based on transferred PtSe<sub>2</sub> films grown by VPT, Wang et al. demonstrated 17GHz-bandwidth photodetectors fabricated on a SiO<sub>2</sub>/Si substrate<sup>[19]</sup> and 35GHz-bandwidth waveguide photodetectors realized on a silicon

nitride platform.<sup>[20]</sup> In these experiments, semimetallic PtSe<sub>2</sub> acts as a photoconductor as the 1.55  $\mu\text{m}$  light absorption leads to the increase in carrier density and further, to the increase in conductance.<sup>[9]</sup> A photoconductor is generally not considered to be an efficient photodetector because it requires a DC bias to measure the change in conductance, which results in a “dark” current, inducing power consumption. In contrast, a photoconductor is well suited to optoelectronic mixing, making PtSe<sub>2</sub> a good candidate for this application. In fact, in order to mix the input RF signal and the optical power, it is essential that the photodetected signal depends on both the optical power and the channel bias. When operating as an optoelectronic mixer (OEM), no DC bias is required as the PtSe<sub>2</sub> channel bias is provided by the input RF signal. OEMs are key components, especially in telecommunications,<sup>[21]</sup> where signals with a high-frequency carrier need to be down-converted at the receiver. As data transmission increases rapidly, new technologies such as 6G aim to increase the signal bandwidth ( $> 0.5$  GHz) and carrier frequency ( $>10$  GHz), requiring high-frequency OEMs. To date, 2D-based OEMs have been demonstrated with single layer graphene.<sup>[22,23,24,25]</sup> Indeed, it has been shown that high mobility and efficient photodetection (at 1.55  $\mu\text{m}$ ) are mandatory properties to demonstrate high-performance OEMs.<sup>[24]</sup> Concerning the OEMs based on graphene, the higher the carrier mobility, the higher the conductivity and the higher the photoconductivity.<sup>[24]</sup> Compared to single layer graphene, multilayer PtSe<sub>2</sub> has a lower carrier mobility but a higher IR absorption, which can be easily enhanced by increasing the number of layers.<sup>[9,26,27]</sup> In contrast, the growth of multilayer graphene with precise thicknesses and controlled electronic properties remains a critical challenge.<sup>[28]</sup> Multilayer semimetallic PtSe<sub>2</sub> appears to be an excellent candidate to outperform the IR OEMs based on 2D materials.

The thickness-dependent electronic properties of PtSe<sub>2</sub> have been extensively investigated by theoretical calculations<sup>[8,29,30]</sup> and experimental studies. Experimental observations have shown that PtSe<sub>2</sub> exhibits an indirect bandgap of  $\sim 2$  eV for a monolayer (1 ML), which decreases to 0.6 - 1.1 eV for the bilayer,<sup>[31,32]</sup> and is semimetallic in the bulk.<sup>[9,33]</sup> However, the semiconductor-to-semimetal transition varies widely in the different reported works: metallic characters have been observed from 3 - 5 MLs,<sup>[14,34]</sup> whereas other works have demonstrated semiconducting behaviors up to 3 to 9 MLs.<sup>[10,30,33,34,35,36]</sup> In addition, the presence of both semiconducting and semimetallic phases has been reported in PtSe<sub>2</sub> films.<sup>[26,27,37]</sup> It could be related to the structural properties of grown PtSe<sub>2</sub> films, which are mostly polycrystalline and could include different stacking polymorphs exhibiting various band structures.<sup>[38]</sup> Therefore, controlling the structural properties of PtSe<sub>2</sub> films appears to be mandatory to understand and optimize their electronic properties.

Due to these excellent electronic and optoelectronic properties, large research efforts have been devoted to the controlled synthesis of 2D PtSe<sub>2</sub>. These include mechanical/liquid phase exfoliation,<sup>[14,33,39,40,41,42,43]</sup> vapor phase transport (VPT),<sup>[14,26,27,44]</sup> selenization of a pre-deposited platinum film in a tube configuration<sup>[11,34,36,37,45,46]</sup> or in a molecular beam epitaxy (MBE) reactor<sup>[12,47,48]</sup> and the “standard” MBE process with simultaneous platinum (Pt) and selenium (Se) fluxes.<sup>[12,31,32,49,50]</sup> However, the growth of high crystalline quality PtSe<sub>2</sub> films on low cost and insulating substrates, suitable to (opto)electronic devices, is still a challenge. To evaluate the crystallinity of PtSe<sub>2</sub>, most groups<sup>[36,37,40,48,50]</sup> have measured the full width at half maximum of the E<sub>g</sub> Raman peak (E<sub>g</sub> FWHM): the thinner the E<sub>g</sub> peak, the higher the crystallinity of the film. E<sub>g</sub> FWHM ≤ 7 cm<sup>-1</sup> was first used as a criterion of high crystalline quality<sup>[40]</sup> and this value was re-evaluated by Lukas et al.<sup>[37]</sup> who proposed an E<sub>g</sub> FWHM ≤ 5 cm<sup>-1</sup> for films grown by selenization in a tube configuration, also called thermally assisted conversion (TAC). The lowest E<sub>g</sub> FWHM values reported for grown PtSe<sub>2</sub> samples have been obtained by this synthesis method and reach 3.5 - 4.1 cm<sup>-1</sup> for 5.5 - 6.5 nm thick (11 - 13 MLs) polycrystalline films.<sup>[36]</sup> Concerning the MBE method, Hilse et al.<sup>[48]</sup> have synthesized polycrystalline PtSe<sub>2</sub> films on sapphire(0001), with E<sub>g</sub> FWHM values down to 7 cm<sup>-1</sup>, by the selenization of Pt films and have significantly improved the crystalline quality using simultaneous Pt and Se fluxes: the reported value decreases to 5.2 cm<sup>-1</sup> for a 10 nm thick film (20 MLs).<sup>[50]</sup> The advantages of MBE over other growth methods are that it allows a more precise control of the various parameters throughout the growth process, and enables obtaining epitaxial PtSe<sub>2</sub> films on specific substrates such as Pt(111), bilayer graphene/6H-SiC(0001) and ZnO(0001),<sup>[12,47,49]</sup> but the corresponding E<sub>g</sub> FWHM values have not been reported. For studies including those targeting epitaxial PtSe<sub>2</sub> films, the experimental carrier mobility values remain considerably lower (≤ 200 cm<sup>2</sup>.(V.s)<sup>-1</sup>)<sup>[12,34,35,36,37,44]</sup> than the predicted intrinsic mobility of PtSe<sub>2</sub> (> 4000 cm<sup>2</sup>.(V.s)<sup>-1</sup>). This indicates that further research efforts are required to achieve highly crystalline and homogeneous films on a large scale, in order to demonstrate high-performance (opto)electronic devices.

In this work, we first study the optical absorption at 1.55 μm and the electrical conductivity of PtSe<sub>2</sub> as a function of the number of layers and we show that thick (≥ 10 MLs) films exhibit both good IR absorption and high conductivity, i.e. the characteristics required for efficient OEMs. Therefore, the synthesis of thick (12 - 16 MLs) semimetallic PtSe<sub>2</sub> films by MBE on sapphire(0001) substrates is investigated. Sapphire was chosen because it is particularly well suited for optoelectronic applications: it is a low cost, insulating and transparent substrate available in sizes up to 12 inches. The effects of the growth temperature,

post-growth annealing and Se flux on the crystalline quality of PtSe<sub>2</sub> films are first studied by monitoring the evolution of the commonly used E<sub>g</sub> FWHM, but also of the A<sub>1g</sub> FWHM. Optimized as-grown films exhibit low FWHM values for both the E<sub>g</sub> peak ( $\leq 4 \text{ cm}^{-1}$ ) and the A<sub>1g</sub> peak ( $< 5 \text{ cm}^{-1}$ ). A post-growth annealing further improves the crystallinity of the films, with E<sub>g</sub> and A<sub>1g</sub> FWHM values decreasing to only  $3.6 \text{ cm}^{-1}$  and  $3.5 \text{ cm}^{-1}$ , respectively. This drastic reduction in A<sub>1g</sub> FWHM induced by the annealing process is accompanied by a significant increase in the film conductivity, which rises from 0.5 mS to the maximum value of 1.6 mS. This maximum value is a record for grown films and is equal to the best conductivity reported, which corresponds to exfoliated PtSe<sub>2</sub> of similar thickness,<sup>[33]</sup> demonstrating the importance of high crystallinity for high conductivity. Secondly, in-depth structural analyses using X-ray diffraction (XRD) and scanning transmission electron microscopy (STEM) are performed to clarify the structural factors influencing the E<sub>g</sub> and A<sub>1g</sub> peak widths and to understand their impact on the electrical properties of PtSe<sub>2</sub> films. Non-annealed MBE-grown films consist of three-dimensionally distributed twisted domains, whereas the annealed films consist of a 2D network of vertically single crystalline domains. Therefore, the post-growth annealing process induces remarkable out-of-plane crystalline improvements, monitored by the A<sub>1g</sub> peak width, and leads to record conductivities for grown films, up to 1.6 mS. Compared to previous works<sup>[36,37,40,48,50]</sup> which only analyzed the E<sub>g</sub> FWHM, the present study reveals the particular importance of monitoring both E<sub>g</sub> and A<sub>1g</sub> peak widths as metrics to efficiently evaluate the overall crystalline quality and electrical conductivity of thick PtSe<sub>2</sub> films. Films with the lower E<sub>g</sub> and A<sub>1g</sub> FWHMs exhibit the higher crystallinity in both the in-plane and out-of-plane directions, as well as the higher conductivities. Finally, we fabricate high-frequency 1.55  $\mu\text{m}$  optoelectronic devices on a 2-inch sapphire substrate, based on high quality 14 ML semimetallic PtSe<sub>2</sub> integrated into a coplanar waveguide. We present photodetectors with a record bandwidth of 60 GHz and the first PtSe<sub>2</sub>-based OEM with a bandwidth above 30 GHz.

## 2. Results and discussion

### 2.1. Thickness dependence of PtSe<sub>2</sub> optical absorption and electrical conductivity

In this section, we will study the optical absorption and electrical conductivity of PtSe<sub>2</sub> as a function of the thickness to determine the optimum film thickness for achieving high-performance 1.55  $\mu\text{m}$  OEMs. First, optical measurements were performed on exfoliated PtSe<sub>2</sub>

films transferred to quartz (experimental methods described in Tharrault et al.<sup>[30]</sup>). For each flake, accurate atomic force microscopy (AFM) and Raman analysis allowed us to determine the exact number of layers.<sup>[43]</sup> Then, using the model developed by Li and Heinz,<sup>[51]</sup> we calculated the optical absorption of the different flakes on a sapphire substrate (instead of quartz). The blue dots in **Figure 1a** represent the optical absorption per layer of 1 to 12 MLs of PtSe<sub>2</sub> on sapphire. From 5 MLs, the absorption per layer of exfoliated flakes saturates at around 0.6 %, indicating that the absorption becomes proportional to the number of layers. This value is similar for the 14 ML PtSe<sub>2</sub> film synthesized by MBE (red dot in **Figure 1a**). The inset shows the total absorption of this MBE film as a function of the optical wavelength. The absorption, which is around 35 % in the visible region, decreases in the IR region but still reaches 7.5 % at 1.55  $\mu\text{m}$ . This is a relatively high value compared to a single layer of graphene on sapphire which absorbs only 1.3 % of the incident light.<sup>[51]</sup> Therefore, our 14 ML PtSe<sub>2</sub> absorbs about 6 times more than the graphene.

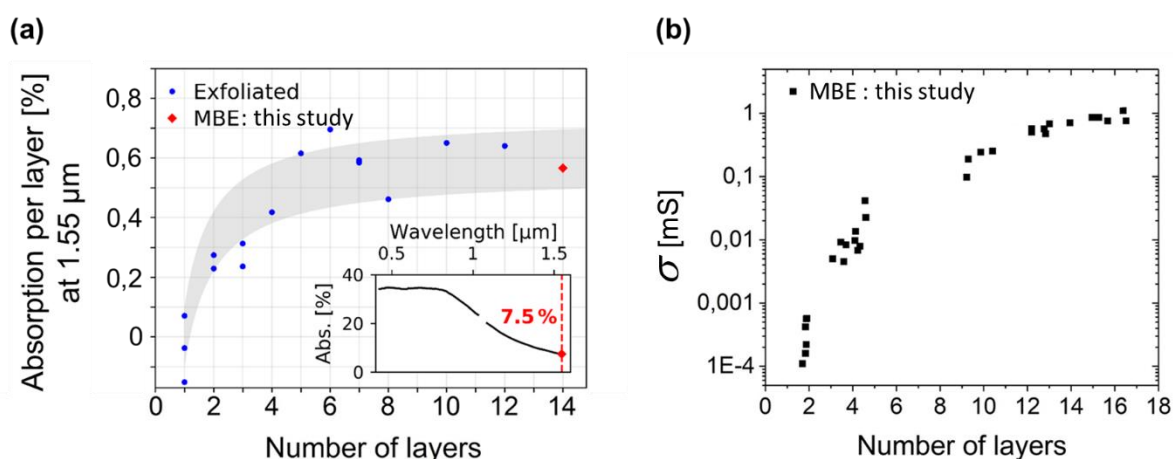


Figure 1. (a) Optical absorption per layer (at 1.55  $\mu\text{m}$ ) of PtSe<sub>2</sub> on sapphire substrate as a function of the number of layers. The blue dots correspond to exfoliated PtSe<sub>2</sub> flakes and the red dot to a 14ML PtSe<sub>2</sub> film synthesized by MBE in this study. The grey area is a guide for the eyes. The inset shows the total optical absorption of this MBE film as a function of the optical wavelength. The dashed red line indicates an absorption of 7.5 % at 1.55  $\mu\text{m}$ . (b) Electrical conductivity of MBE-grown PtSe<sub>2</sub> films on sapphire substrate as a function of the number of layers. The latter was determined by EDX measurements (see details in Figure S1).

Secondly, the electrical conductivity ( $\sigma$ ) of PtSe<sub>2</sub> films synthesized by MBE in this study was investigated as a function of the number of layers (Figure 1b).  $\sigma$  corresponds to the

conductance of a squared shaped PtSe<sub>2</sub> channel, i.e. the inverse of the square resistance ( $R_{\square}$ ). Figure 1b shows that  $\sigma$  is very low for thin (2 to 5 MLs) PtSe<sub>2</sub> films and increases from 0.1 to 1 mS between 9 and 16 MLs. The present study targets the fabrication of IR OEMs based on photoconductive PtSe<sub>2</sub>. For single layer graphene, the higher the conductivity, the higher the photoconductivity.<sup>[24]</sup> Therefore, in order to fabricate efficient IR OEMs, we chose to focus our studies on PtSe<sub>2</sub> films with thicknesses ranging from 12 to 16 MLs, which exhibit both high absorption at 1.55  $\mu\text{m}$  and high conductivity.

## 2.2. Optimization of PtSe<sub>2</sub> synthesis

We have investigated the MBE synthesis of PtSe<sub>2</sub> films on 20 x 20 mm<sup>2</sup> sapphire(0001) substrates (c-plane). During the synthesis, the heated substrate was exposed to Pt and Se fluxes of  $\Phi(\text{Pt}) = 0.003 \text{ \AA}\cdot\text{s}^{-1}$  and  $\Phi(\text{Se}) = 0.2 \text{ \AA}\cdot\text{s}^{-1}$ . The film thickness was determined by energy dispersive X-ray spectroscopy (EDX) (see details in Figure S1). Raman spectroscopy ( $\lambda = 532 \text{ nm}$ ) was used to characterize the crystalline quality of samples. The recorded spectra exhibit the two characteristic peaks of PtSe<sub>2</sub> (Figure 2a): the  $E_g$  peak at  $\sim 178 \text{ cm}^{-1}$  and the  $A_{1g}$  peak at  $\sim 206.5 \text{ cm}^{-1}$ , corresponding respectively to the in-plane and the out-of-plane motion of Se atoms in opposite directions within a monolayer.<sup>[45]</sup> They also show a broad feature centered at  $\sim 235 \text{ cm}^{-1}$ , attributed to the longitudinal optical (LO) mode, which is a combination of two IR-active modes named  $A_{2u}$  and  $E_u$ .<sup>[45]</sup> Figure 2b presents the median values of the  $E_g$  and  $A_{1g}$  FWHMs as a function the growth temperature (Tg), varying between 329 and 747 °C. The vertical bars correspond to the interquartile values of the FWHMs and represent the inhomogeneity of the PtSe<sub>2</sub> films (see Methods section). The lowest  $E_g$  FWHM values (3.7 - 4.0  $\text{cm}^{-1}$ ), commonly attributed to the highest crystalline quality,<sup>[36,37,40]</sup> are obtained for samples grown at Tg between 463 and 570 °C. Above or below these temperatures, the  $E_g$  FWHM values increase above 4.5  $\text{cm}^{-1}$ , indicating a deterioration in the film crystallinity. Note that the  $A_{1g}$  FWHM values follow exactly the same trend.

EDX measurements were performed on these films to extract the atomic ratio of Se/Pt (Figure 2c). Samples grown at Tg between 463 and 570 °C exhibit the highest ratios, between 1.85 and 1.92. Such values smaller than 2 (PtSe<sub>2</sub> stoichiometry) are generally obtained on grown films.<sup>[14,36]</sup> Samples synthesized at Tg below 463 °C present slightly lower Se/Pt ratios (1.75 and 1.76), indicating higher Se deficiency. This ratio drops to 0.67 for films grown at Tg = 597 °C and stabilizes at 0.4 around 700 °C. Note that at Tg = 597 °C, a strong dispersion of both the  $E_g$  and  $A_{1g}$  FWHM values is observed (large vertical bars in Figure 2b), indicating a

strong film inhomogeneity, as shown in Figure S2(c-d). These results demonstrate that the limit growth temperature of PtSe<sub>2</sub> with  $\Phi(\text{Se}) = 0.2 \text{ \AA}\cdot\text{s}^{-1}$  lies between 570 and 597 °C. The abrupt decrease in the Se/Pt ratio for  $T_g \geq 597 \text{ °C}$  can be explained by the small Se sticking coefficient, which decreases exponentially with increasing temperature.<sup>[52]</sup> It could also be caused by a phase change. Indeed, Tong et al.<sup>[53]</sup> observed a phase change from PtSe<sub>2</sub> to Pt<sub>2</sub>Se alloy monolayer structure at temperatures above 600 °C. Therefore, Figure 2 demonstrates that high quality PtSe<sub>2</sub> films ( $E_g$  FWHM  $\leq 4 \text{ cm}^{-1}$  and  $A_{1g}$  FWHM  $\leq 4.5 \text{ cm}^{-1}$ ) can be synthesized using simultaneous Pt and Se fluxes ( $\Phi(\text{Se})/\Phi(\text{Pt}) \sim 70$ ) over a wide range of temperature (between 463 and 570 °C).

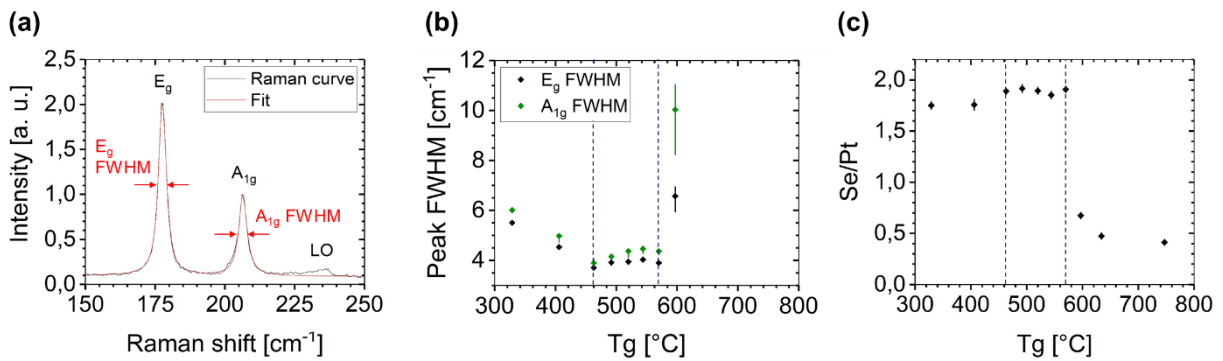


Figure 2. (a) Typical Raman spectrum ( $\lambda = 532 \text{ nm}$ ) of a PtSe<sub>2</sub> film (black curve) showing the  $E_g$  in-plane mode, the  $A_{1g}$  out-of-plane mode and the LO mode. The intensity is normalized to the  $A_{1g}$  peak. The  $E_g$  and  $A_{1g}$  peaks are fitted with Lorentzian functions (the red curve represents the sum of the two fits) to extract the FWHM values. (b) FWHM values of the  $E_g$  peak (black dots) and the  $A_{1g}$  peak (blue dots) of PtSe<sub>2</sub> films synthesized at different growth temperatures ( $T_g$ ) under a Se flux of  $0.2 \text{ \AA}\cdot\text{s}^{-1}$ . The dots are median values and the vertical bars correspond to the interquartile values. From  $T_g = 634 \text{ °C}$ , the Raman signal of PtSe<sub>2</sub> samples becomes very weak (see Figure S2(a-b)) and it was not possible to extract accurate peak FWHM values. (c) Se/Pt atomic ratios of the corresponding samples measured by EDX. Here, the vertical bars correspond to the error on the Se/Pt values.

To further improve the crystalline quality of our PtSe<sub>2</sub> films, we have fixed the growth temperature at  $T_g = 520 \text{ °C}$  and studied the effects of the Se flux and post-growth annealing on the Raman peaks. The Se flux was varied between  $0.1$  and  $0.5 \text{ \AA}\cdot\text{s}^{-1}$  (the Pt flux was kept at  $0.003 \text{ \AA}\cdot\text{s}^{-1}$ ). The annealing was performed at  $T_a = 690 \text{ °C}$  for 30 min under the same Se flux



used during growth. The film thickness varies between 12 and 16 MLs, as shown in Figure 3c. Figure 3 compares the Raman data of PtSe<sub>2</sub> films grown without and with this post-growth annealing. Figure 3a shows the E<sub>g</sub> FWHM values as a function of the Se flux. Irrespective of the Se flux used, annealed samples exhibit lower E<sub>g</sub> FWHM values than samples synthesized without annealing (as-grown samples). In addition, the E<sub>g</sub> FWHM values of the annealed samples decrease slightly with increasing the Se flux: from 4.0 cm<sup>-1</sup> at 0.1 Å.s<sup>-1</sup> to only 3.6 - 3.7 cm<sup>-1</sup> at 0.5 Å.s<sup>-1</sup>. Increasing the Se flux does not significantly modify the Se/Pt atomic ratio measured by EDX and there is also no obvious change in this ratio between as-grown and annealed samples (see Figure S3), demonstrating that no desorption of Se occurs during the post-growth annealing under Se flux. Comparing Figure 3b with Figure 3a shows that the main effect of the post-growth annealing is a strong reduction in the FWHM of the out-of-plane A<sub>1g</sub> mode, regardless of the Se flux. For example, at a Se flux of 0.5 Å.s<sup>-1</sup> the A<sub>1g</sub> FWHM drops from 4.3 - 4.7 cm<sup>-1</sup> to 3.5 - 3.8 cm<sup>-1</sup> with the annealing. Therefore, by comparing the E<sub>g</sub> and A<sub>1g</sub> FWHMs of the as-grown and annealed samples, we demonstrate that the post-growth annealing improves the crystalline quality of PtSe<sub>2</sub> films. The lowest FWHM values of both peaks are obtained for the annealed samples synthesized under 0.5 Å.s<sup>-1</sup> of Se, indicating that the higher the Se flux, the higher the crystalline quality.

Hilse et al.<sup>[50]</sup> have also studied the MBE synthesis of thick PtSe<sub>2</sub> films on sapphire substrate and have obtained E<sub>g</sub> and A<sub>1g</sub> FWHM values of 5.2 and 6.5 cm<sup>-1</sup>, respectively. Compared to this study, we have implemented higher Φ(Se)/Φ(Pt) ratios (33 - 170 instead of 20), performed the growth at 520 °C instead of 200 °C and annealed the films at 690 °C instead of 400 °C. These elevated temperatures and Se fluxes result in as-grown and annealed samples exhibiting much lower FWHM values. Our annealed MBE samples synthesized under 0.5 Å.s<sup>-1</sup> of Se present E<sub>g</sub> and A<sub>1g</sub> FWHM down to ~ 3.5 cm<sup>-1</sup>, approaching the values obtained with thick exfoliated films, ranging between 2.6 and 3.8 cm<sup>-1</sup> for the E<sub>g</sub> peak.<sup>[40,42,43]</sup>

Figure 3c compares the intensity ratio between the A<sub>1g</sub> and E<sub>g</sub> peaks (I(A<sub>1g</sub>)/I(E<sub>g</sub>)) as a function of the number of layers. The slight increase in this ratio with increasing the film thickness has been observed previously<sup>[36,40,43,45,49,50]</sup> and explained by enhanced van der Waals (vdW) interlayer interactions.<sup>[45,49]</sup> Annealed samples exhibit a much higher ratio (~ + 40 %) compared to as-grown samples showing that the crystalline quality also strongly influences I(A<sub>1g</sub>)/I(E<sub>g</sub>).<sup>[50]</sup> Most of the studies have investigated the evolution of this ratio as a function of the film thickness of PtSe<sub>2</sub> samples,<sup>[36,40,43,45,49]</sup> however we demonstrate that this should be performed only with samples of the same crystalline quality.

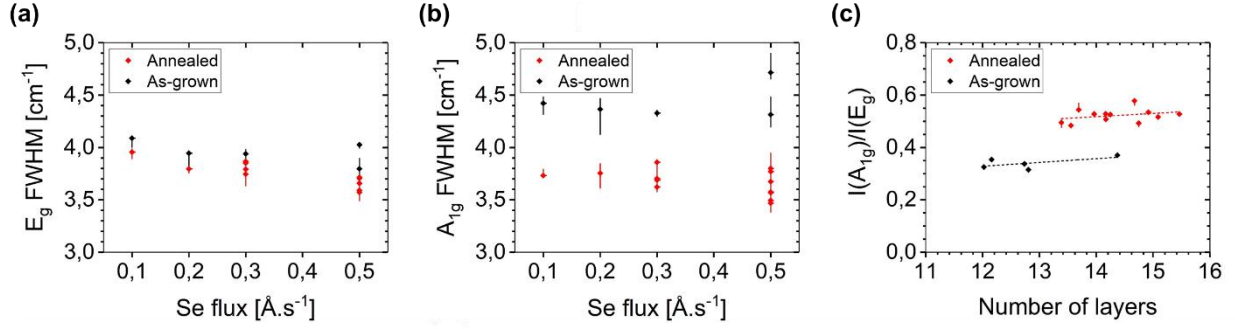


Figure 3. Raman analyses ( $\lambda = 532$  nm) of MBE-grown  $\text{PtSe}_2$  films. Samples are synthesized at  $520$  °C without (black dots) or with (red dots) a post-growth annealing at  $690$  °C for 30 min, under different Se fluxes. 7 annealed samples were prepared under a Se flux of  $0.5$   $\text{\AA}\cdot\text{s}^{-1}$  to study the reproducibility of the synthesis. The dots are median values and the vertical bars correspond to the interquartile values. FWHM values of (a) the  $E_g$  peak and (b) the  $A_{1g}$  peak as a function of the Se flux. (c) Intensity ratio between the  $A_{1g}$  and  $E_g$  peaks ( $I(A_{1g})/I(E_g)$ ) as a function of the number of layers. The latter was determined by EDX measurements (see details in Figure S1).

The electrical conductivity ( $\sigma$ ) of these  $\text{PtSe}_2$  films was also studied (Figure 4). We selected samples of similar thickness: 12 - 13 MLs for as-grown samples and 14 - 15 MLs for annealed samples. Both as-grown and annealed samples exhibit purely ohmic behaviors. Figure 4a shows that  $\sigma$  is similar for the as-grown samples and equal to  $0.5 - 0.6$  mS, irrespective of the Se flux. In contrast,  $\sigma$  of the annealed samples is much higher and increases with the Se flux (red dashed line): it goes from  $1.17$  mS for  $0.1$   $\text{\AA}\cdot\text{s}^{-1}$  to  $1.36 - 1.59$  mS for  $0.5$   $\text{\AA}\cdot\text{s}^{-1}$ . Figure S4 shows that these measured conductivities appear to be well above the reported values ( $\leq 0.3$  mS) for grown  $\text{PtSe}_2$  films, and that our maximal value of  $1.6$  mS is as high as the best value reported for exfoliated  $\text{PtSe}_2$  of similar thickness (8 nm i.e.  $\sim 16$  MLs).<sup>[33]</sup>

Figure 4b and 4c present  $\sigma$  as a function of the  $E_g$  FWHM and  $A_{1g}$  FWHM, respectively. Concerning the annealed samples,  $\sigma$  increases as the FWHM of both the  $E_g$  and  $A_{1g}$  peaks decreases, with a very similar slope. However, Figure 4b shows that as-grown and annealed films with similar  $E_g$  FWHM values can exhibit different  $\sigma$  values. In contrast, in Figure 4c we observe that the conductivity of the same films can be fitted as a linear function of  $A_{1g}$  FWHM. Note that Lukas et al.<sup>[37]</sup> have measured an exponential dependence of the  $R_{\square}$  on the  $E_g$  FWHM

for TAC-grown films which exhibit  $E_g$  FWHM between 4.3 and 8  $\text{cm}^{-1}$ . Therefore, we suggest that both the  $E_g$  and  $A_{1g}$  FWHM values should be considered as indicators of film conductivity. Finally, Figure 4 clearly demonstrates that the post-growth annealing at high temperature significantly increases the electrical conductivity of  $\text{PtSe}_2$  films. Our annealed MBE samples synthesized under 0.5  $\text{\AA}\cdot\text{s}^{-1}$  of Se exhibit the highest conductivities. Our optimum growth conditions are  $T_g = 520\text{ }^\circ\text{C}$ ,  $T_a = 690\text{ }^\circ\text{C}$  and  $\Phi(\text{Se})/\Phi(\text{Pt}) = 170$ .

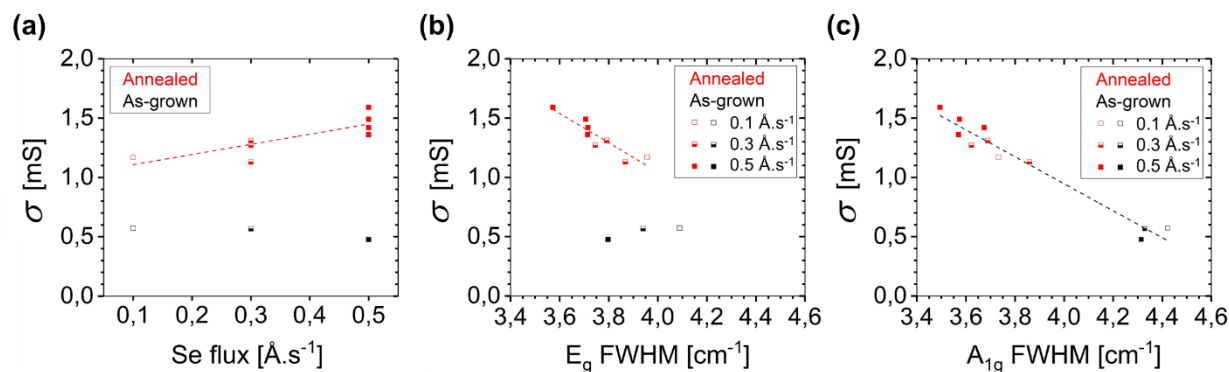


Figure 4. Electrical conductivity ( $\sigma$ ) of MBE-grown  $\text{PtSe}_2$  films (12 - 15 MLs). Samples are synthesized at 520  $^\circ\text{C}$  without (black dots) or with (red dots) a post-growth annealing at 690  $^\circ\text{C}$  for 30 min, under different Se fluxes.  $\sigma$  is plotted as a function of (a) the Se flux, (b) the  $E_g$  FWHM and (c) the  $A_{1g}$  FWHM. Empty, half-empty and full squares correspond to Se fluxes of 0.1, 0.3 and 0.5  $\text{\AA}\cdot\text{s}^{-1}$ , respectively.

The air stability of thick  $\text{PtSe}_2$  films was investigated using Raman spectroscopy, EDX and conductivity measurements. Figure S5a shows the Raman spectra recorded on an annealed sample a few days after the synthesis and after 1.5 years in air. The spectra are similar, as well as the median values of both the  $E_g$  and  $A_{1g}$  FWHMs. There is also no significant change in the Se/Pt ratio after 1.5 years in air (Figure S5(b-c)). Finally,  $\sigma$  of the film a few days after the synthesis and after 1.5 years in air is 1.49 mS and 1.46 mS, respectively. Therefore, the crystalline quality and electrical conductivity of multilayer  $\text{PtSe}_2$  are preserved after 1.5 years in air, demonstrating the excellent stability of this 2D material and its great potential for device applications.

### 2.3. XRD and STEM structural characterizations on as-grown and annealed samples

In-depth structural analyses were carried out on PtSe<sub>2</sub> films synthesized at 520 °C without and with a post-growth annealing at 690 °C under 0.5 Å.s<sup>-1</sup> of Se (as-grown and annealed films, respectively). XRD and STEM techniques are implemented to determine the structural changes induced by the post-growth annealing, which drastically reduces A<sub>1g</sub> FWHM and increases film conductivity.

First, PtSe<sub>2</sub>/sapphire(0001) samples were characterized at the macroscopic scale by grazing incidence X-ray diffraction (GIXRD) measurements. Bragg scans along the in-plane Al<sub>2</sub>O<sub>3</sub><11-20> direction were performed on both films. Figure 5a shows that only crystallographic planes with Miller index *l* = 0 are observed, implying that the two films are fiber textured with c-planes parallel to the substrate surface. The azimuthal  $\varphi$  scan (Figure S6) across the PtSe<sub>2</sub>[11-20] direction confirms the fiber texture with domains exhibiting random in-plane orientations. Bragg scans also provide useful information on the in-plane lattice parameters and domain sizes. Considering a hexagonal crystal symmetry, the in-plane lattice parameter “a” is calculated to be equal to 3.698 ± 0.002 Å and 3.716 ± 0.001 Å for the as-grown and annealed samples, respectively. Thus, the post-growth annealing induces an increase in the lattice parameter, approaching the experimental value of 3.727 Å measured for bulk monocrystalline PtSe<sub>2</sub>.<sup>[54]</sup> We implemented the Williamson-Hall method<sup>[55]</sup> to evaluate the contribution of the in-plane domain size (D<sub>WH</sub>) and the lattice microstrain (ε) to the broadening of the diffraction peaks (see details in Table S1 and S2). According to this method:

$$\Delta(2\theta_\chi)\cos(\theta_\chi) = \frac{K\lambda}{D_{WH}} + 4\epsilon\sin(\theta_\chi)$$

where 2θ<sub>χ</sub> is the diffraction angle, Δ(2θ<sub>χ</sub>) is the diffraction peak FWHM deconvoluted from the instrument width, K is the Scherrer constant (0.94 for isotropic crystallites) and λ is the X-ray wavelength (1.54056 Å).

In Figure 5b, Δ(2θ<sub>χ</sub>)cos(θ<sub>χ</sub>) is plotted as a function of sin(θ<sub>χ</sub>) and fitted with a linear function. For both the as-grown and annealed samples, the experimental data are well fitted by lines, as predicted by the method. From the slope and y-intercept, we derive D<sub>WH</sub> and ε values of 724 ± 54 Å and 0.38 % for the as-grown film and 630 ± 107 Å and 0.22 % for the annealed film (Table S2). Thus, the in-plane domain size is approximately the same for the as-grown and annealed samples and the main effect of the post-growth annealing is an important reduction in the non-uniform in-plane lattice distortions, by a factor of almost 2. The observed local microstrains can be due to point defects and/or dislocations, suggesting that the defect density is lower in the annealed sample compared to the as-grown sample.<sup>[56]</sup>

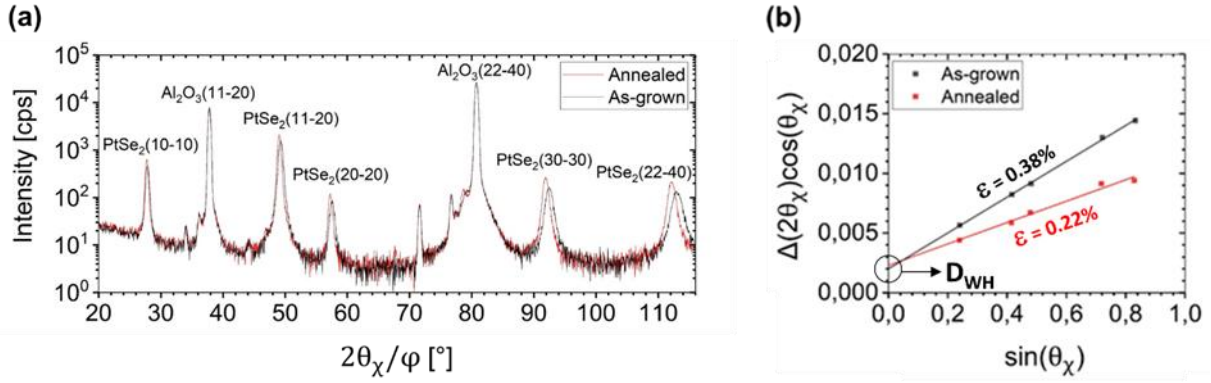


Figure 5. (a) GIXRD Bragg scans of the as-grown and annealed PtSe<sub>2</sub> films along the in-plane Al<sub>2</sub>O<sub>3</sub><11-20> direction. The FWHM of the five PtSe<sub>2</sub>(hki0) diffraction peaks ( $\Delta(2\theta_\chi)_{\text{meas}}$ ) are extracted by fitting them with PearsonVII functions (Table S1). (b) Calculation of the in-plane domain size ( $D_{\text{WH}}$ ) and lattice microstrain ( $\epsilon$ ) using a Williamson-Hall plot applied to these five diffraction peaks (see details in Table S1 and S2).

Figure 6 shows the high-resolution X-ray diffraction (HRXRD)  $2\theta/\omega$  Bragg scans collected on the as-grown and annealed samples. As expected, only the PtSe<sub>2</sub> diffraction peaks corresponding to crystallographic planes with Miller indices  $h = k = 0$  are detected. The PtSe<sub>2</sub> diffraction peaks, as well as the fringes around the PtSe<sub>2</sub>(0001) are better defined for the annealed sample compared to the as-grown sample. According to the positions of the diffraction peaks, the out-of-plane lattice parameter “c” is lower for the annealed sample compared to the as-grown sample,  $5.165 \pm 0.02 \text{ \AA}$  compared to  $5.300 \pm 0.10 \text{ \AA}$ , and approaches the value of bulk monocrystalline PtSe<sub>2</sub> ( $5.07 \text{ \AA}$ ).<sup>[54]</sup> The asymmetric shape of the diffracted peaks is more pronounced in the as-grown sample, with a tail towards the low angles, revealing a gradual lattice parameter “c” towards higher values. Therefore, HRXRD analyses show that the annealed sample presents a higher out-of-plane crystalline quality and exhibits a smaller and more uniform interlayer distance compared to the as-grown sample.

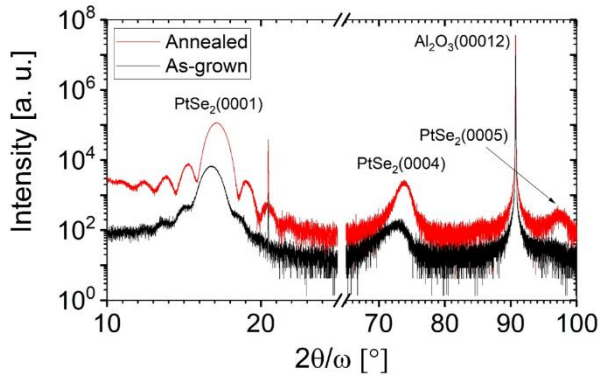
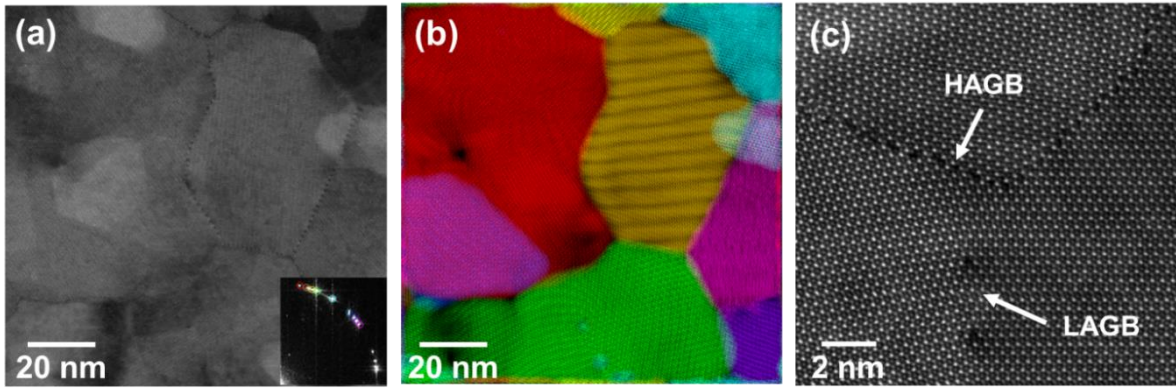


Figure 6. HRXRD Bragg scans of the as-grown and annealed PtSe<sub>2</sub> films along the Al<sub>2</sub>O<sub>3</sub><0001> direction.

**Post-growth annealed sample**



**As-grown sample**

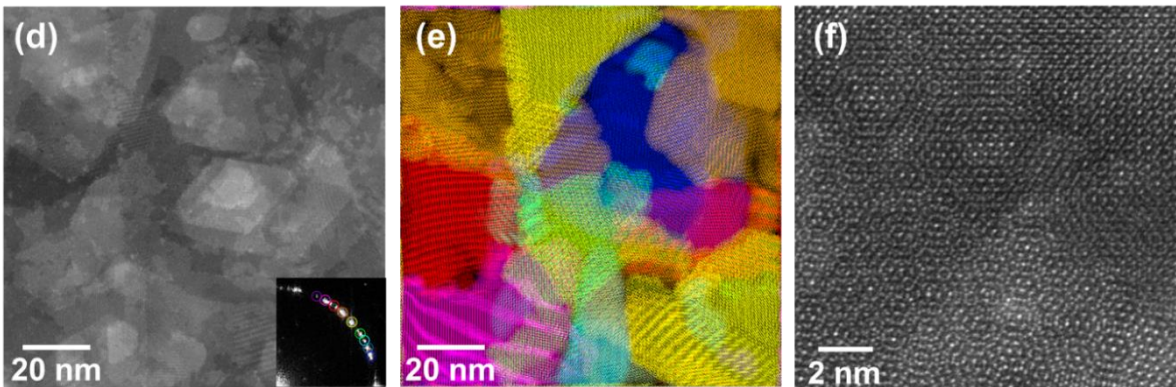


Figure 7. (a) HAADF-STEM image of the annealed sample with (b) the corresponding FFT-based composite DF image. (c) Typical HAGB and dislocations aligned as LAGB. (d) HAADF-STEM image of the as-grown sample with (e) the corresponding FFT-based composite DF image and (f) the typical moiré structures. The color code used for the DF images is given in the FFT in the inset of their original HAADF images.

Second, the detailed structural properties of the PtSe<sub>2</sub> films were investigated using STEM. Figure 7a shows a plan-view high angle annular dark field (HAADF) image of the annealed film. Figure 7b is a composite dark field (DF) image reconstructed using the Fast Fourier Transform (FFT), where each color represents an in-plane orientation indicated in the inset of Figure 7a. Atomic resolution analysis (Figure 7c) identified highly crystalline domains exhibiting random in-plane orientations. They are laterally connected either with continuous line defects, so called high angle grain boundaries (HAGBs) or isolated dislocation cores defining low angle grain boundaries (LAGBs) (see detailed GB structures in Figure S7). Considering the PtSe<sub>2</sub> film thickness (~ 14 MLs), the perfect vertical alignment of the crystal lattice as well as the GBs and dislocations within the film thickness demonstrates a single crystalline character along the c-axis. STEM image analyses (Figure 7b and Figure S8) revealed that most of crystalline domains have in-plane sizes falling within the range of 50 - 80 nm. In the as-grown sample, domain boundaries are not clearly identified in the HAADF image (Figure 7d). The composite DF image (Figure 7e) and the atomic resolution image (Figure 7f) suggest that several domains with different in-plane orientations are superimposed, resulting in complex moiré structures. The domain sizes, as defined by the DF images for specific in-plane orientations, are also found to be approximately in the range of 50 - 80 nm (Figure S8). This indicates that the annealing process induces no obvious change in the in-plane domain size, in good agreement with the GIXRD measurements. Contrary to the annealed sample, a slight variation in the local in-plane orientation is often investigated within the identified individual domains of the as-grown film, suggesting a relatively low crystallinity with the presence of point defects and dislocations (see detailed domain analysis of the as-grown sample in Figure S8).

### Post-growth annealed sample

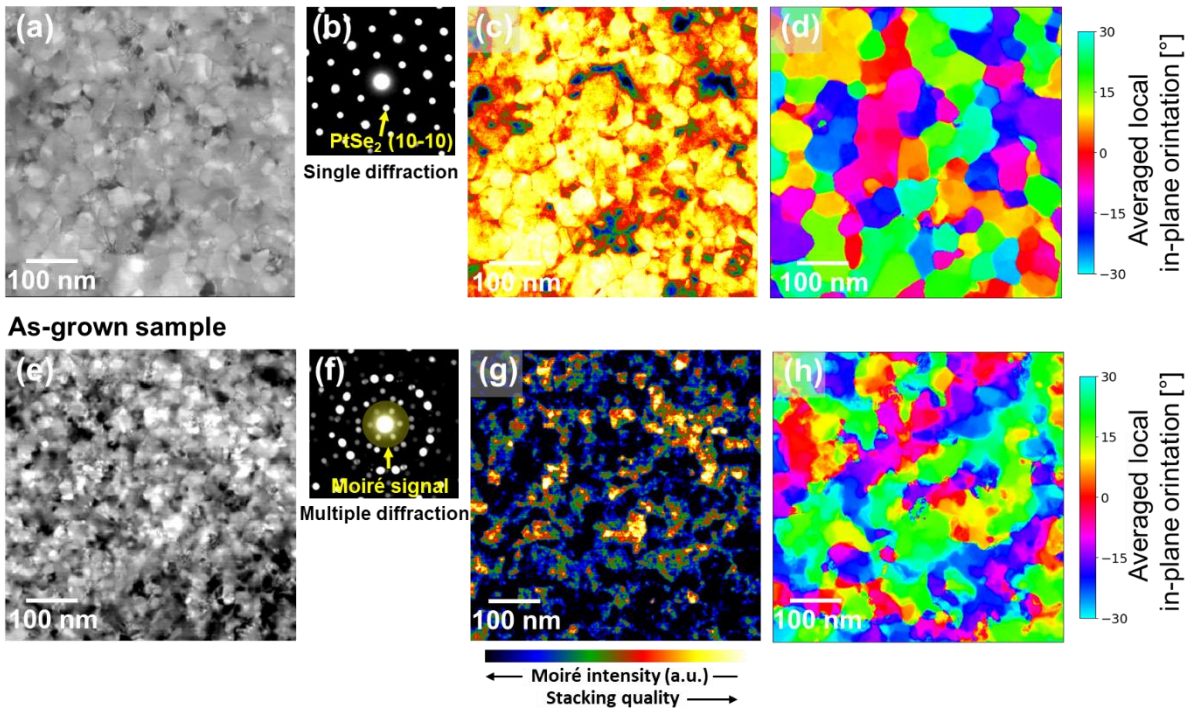


Figure 8. Structural maps reconstructed from the 4D diffraction datasets of the annealed and as-grown samples. (a, e) Virtual ADF images. Typical diffraction patterns observed on (b) the annealed and (f) as-grown samples, where the annular filter used to collect the moiré signals is indicated in yellow. (c, g) Inverse of the moiré intensity map highlighting the vertically well aligned regions. (d, h) Locally averaged in-plane orientation maps.

We have then carried out 4D-STEM analyses to investigate the distribution of the crystalline domains in the PtSe<sub>2</sub> films. An electron diffraction pattern was recorded at each pixel of the electron beam scanning (400 x 400 pixels) over sub-micron areas (~ 570 x 570 nm<sup>2</sup>). Figure 8a and 8e display virtual ADF images reconstructed from the 4D diffraction datasets which represent the analyzed areas of the annealed and as-grown samples, respectively. In order to screen the vertically single crystalline domains, the moiré signal in the diffraction patterns was used. When multiple in-plane orientations are present in a given pixel, additional diffraction spots appear, corresponding to moiré structures. The total intensity collected between the transmitted beam and the PtSe<sub>2</sub>(10-10) ring (Figure 8f), defined as the moiré intensity, can be related to the local vertical misalignment in the depth of the film (see experimental details and moiré intensity maps in Figure S9). The inverse of the moiré intensity, shown in Figure 8c and 8g, allows identifying the vertically well aligned regions, with no or few moiré signals, highlighted in yellow. It is used to assess the stacking quality of the



multilayer PtSe<sub>2</sub> films. In-plane orientation maps (Figure 8d and 8h) are also reconstructed by measuring the direction of the hexagonal symmetry in the diffraction pattern recorded at each pixel of the scan areas. When multiple ( $> 2$ ) hexagonal diffractions are present at the same position, an average in-plane angle is calculated, taking into account the intensity of each spot. Figure 8c demonstrates that the annealed sample exhibits fairly well vertically aligned domains over a large area, with few misaligned regions around domain junctions. As most of the domains present a single in-plane orientation within the depth, with a single diffraction pattern as shown in Figure 8b and S9b, the individual domains are relatively well defined by the color codes of the in-plane orientation map in Figure 8d. These maps show a horizontal and uniform distribution of the vertically single crystalline domains constituting the film. For the as-grown film, which exhibits only few vertically aligned regions, as shown in Figure 8g, multiple diffraction spots are observed at most of beam positions with typically 2 to 4 different in-plane orientations (Figure 8f and Figure S9(e-f)). This indicates the presence of 2 to 4 twisted domains superimposed within the film thickness. It should be noted that the colors on the map in Figure 8h correspond to the average of multiple in-plane orientations present within the depth, but not to the real in-plane orientation of the individual domains. To further resolve the in-plane orientation of the individual domains in the film, DF imaging was performed from the same 4D diffraction datasets using a filter of  $7.5^\circ$  width for both the two samples (Figure S10 and S11). Contrary to the annealed sample, several domains with different in-plane orientations are often overlapped at the same position in the as-grown sample. These observations clearly demonstrate a three-dimensional random distribution of twisted domains throughout the volume of the as-grown film.

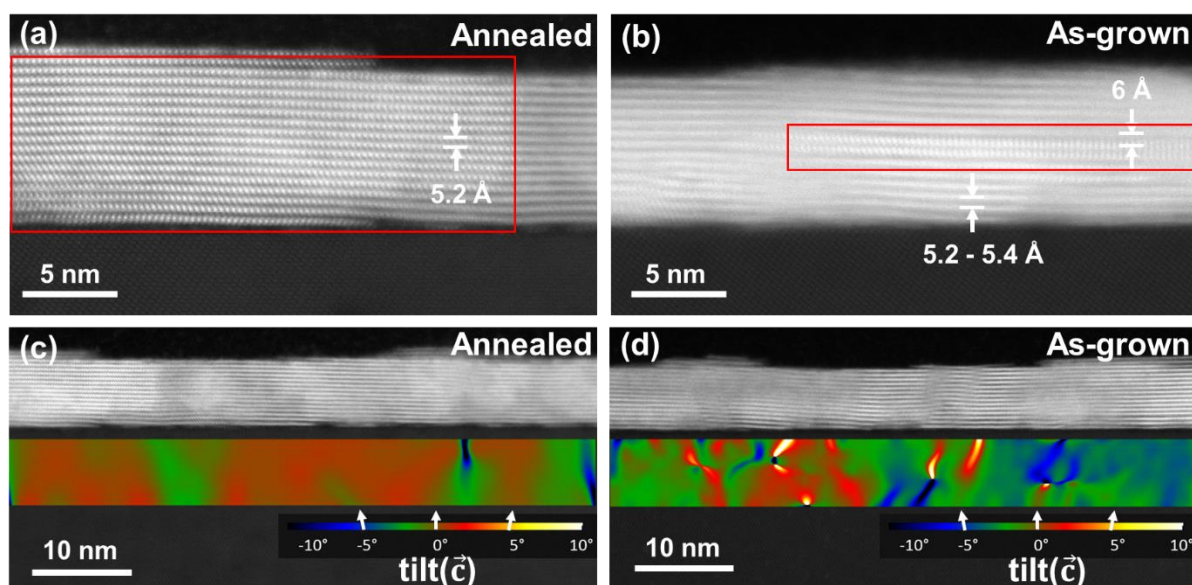


Figure 9. Cross-sectional HAADF-STEM images of (a) the annealed and (b) as-grown samples. Single domains oriented in a zone axis are indicated by red squares. Typical film morphologies of (c) the annealed and (d) as-grown samples. The local tilt angle between PtSe<sub>2</sub> and sapphire c-planes, tilt( $\vec{c}$ ), was determined by GPA using the PtSe<sub>2</sub>(0001) spot. The corresponding tilt( $\vec{c}$ ) map is displayed below each cross-sectional image. Intense vertical lines appear due to the interface effects.

Cross-sectional STEM analyses were carried out to investigate the out-of-plane morphology of the films. Figure 9a and 9b show atomic resolution HAADF-STEM images of typical structures investigated in the annealed and as-grown samples, respectively. In the annealed film, each PtSe<sub>2</sub> layer is horizontally connected to those in neighboring domains. Each single domain consists of flat PtSe<sub>2</sub> layers parallel to each other, with an average interlayer distance of 5.2 Å, with quite small variations. In Figure 9a, a crystalline domain recognized in a zone axis (surrounded by the red square) exhibits vertically single crystalline feature, where the domain thickness corresponds to the film thickness. This confirms a two-dimensional arrangement of highly crystalline domains with a perfect horizontal conjunction. In the as-grown film, each PtSe<sub>2</sub> layer is also horizontally connected, forming a continuous film. However, ruptures in the crystal structure within the film thickness are often identified by increased interlayer distances, supposed to be boundaries between superimposed twisted domains. This is confirmed in Figure 9b where a single crystal domain composed of 2 MLs oriented in a zone axis (surrounded by the red square) is separated from the upper and lower domains by an in-plane misorientation and an increased interlayer distance. The interlayer distance varies between 5.2 and 5.4 Å within areas considered as an individual domain, indicating a relatively low crystallinity, and increases to up to 6 Å between domains. These results clearly show the higher local out-of-plane disorders in the as-grown sample with a higher and non-uniform interlayer distance value, compared to the annealed sample. This is in good agreement with the HRXRD 2 $\theta$ / $\omega$  Bragg scan showing asymmetric peak shapes shifted towards low angles (i.e. high interlayer distance) for the as-grown sample (Figure 6).

Cross-sectional STEM images (Figure 9c and 9d) are also used to extract information on the local out-of-plane misorientation. The local tilt angle of the PtSe<sub>2</sub> c-plane relative to the sapphire c-planes, tilt( $\vec{c}$ ), is determined by FFT-based Geometric Phase Analysis (GPA) using the PtSe<sub>2</sub>(0001) spot.<sup>[57,58]</sup> This allowed to generate orientation field maps, which are shown below each cross-sectional image in Figure 9c and 9d. In the annealed film, the variation in

tilt( $\vec{c}$ ) is mainly observed along the in-plane direction, whereas in the as-grown sample, it varies in the volume of the film along both the in-plane and out-of-plane directions. For an efficient and quantitative comparison of out-of-plane tilt disorders between different samples, we determined characteristic standard deviation values of the local c-plane tilt angle, SD tilt( $\vec{c}$ ), over a large area: tilt( $\vec{c}$ ) values are collected on all pixels of orientation field maps generated over a total width of 600 nm (see details in Figure S12). The characteristic SD tilt( $\vec{c}$ ) values are 0.92 ° for the annealed sample and 1.65° for the as-grown sample. The SD tilt( $\vec{c}$ ) value measured from the orientation field maps reflects several structural factors concerning the planarity of the film and its component layers: domain tilt, interlayer parallelism and individual layer flatness. Although the cross-sectional STEM provides a rather local analysis, the characteristic SD tilt( $\vec{c}$ ) value helps evaluating the out-of-plane crystalline quality of the films and reveals a clear improvement in the planarity factors in the annealed sample compared to the as-grown sample.

From our observations, we conclude that a three-dimensional (in-plane and out-of-plane) structural reorganization is induced by the post-growth annealing at high temperature. In particular, the annealing process leads to a drastic improvement in the out-of-plane crystallinity. Moreover, a significant reduction in the defect density and a rearrangement of GBs are also investigated by the GIXRD and STEM analyses. Contrary to 3D bulk systems, the migration of dislocations and GBs in 2D materials takes place through the in-plane displacement of a few atoms around the dislocation cores.<sup>[59]</sup> Such phenomena induced by a thermal treatment have already been reported in graphene and TMDs, which lead to the rearrangement of dislocations and GBs for lower energy configurations,<sup>[60,61]</sup> and also enable the healing of rotational disorders and stacking faults when the binding energy facilitates it.<sup>[62,63,64]</sup> We suggest that during the post-growth annealing, the in-plane defect migration is promoted for the thermal healing of the high density of defects and strong microstrain observed in the as-grown films.<sup>[65,66]</sup> As a result, the disordered dislocations and GBs spread within the as-grown film are rearranged as horizontally well-organized and vertically aligned HAGBs and LAGBs. This healing process is accompanied by the reduction in the out-of-plane tilt disorder and the reduction in the interlayer distance, as well as its variation. More interestingly, these in-plane defect migrations modify the local in-plane orientation, which align individual domains initially twisted and superimposed within the film thickness. These observations emphasize an important role of the interlayer binding energy in such structural modification of multilayer films. It is worth noting that this in-plane crystal reorganization is spatially limited as no obvious difference in the in-plane domain size was observed between as-grown and annealed

samples, whereas the vertical alignment of the domains results in vertically single crystalline domains. Finally, this study revealed the significant increase in the out-of-plane domain size, driven by the post-growth annealing, resulting in the large-scale re-arrangement of the domain distribution within the PtSe<sub>2</sub> multilayer films.

#### 2.4. E<sub>g</sub> and A<sub>1g</sub> FWHMs as metrics for crystalline quality and electrical conductivity

Raman spectroscopy appears to be an effective technique for assessing the crystalline quality and the electrical conductivity of PtSe<sub>2</sub> samples. In addition, this fast and non-destructive characterization method is well suited for systematic analysis. For samples synthesized by TAC, Lukas et al.<sup>[37]</sup> have shown that the E<sub>g</sub> FWHM correlates with the in-plane domain size and the  $R_{\square}$ . In section 2.2 of the present paper, we have demonstrated the particular importance of the A<sub>1g</sub> FWHM to evaluate both the crystalline quality and the conductivity of our MBE PtSe<sub>2</sub> films. In-depth XRD and STEM results presented in section 2.3 can be used to clarify the correlations between the Raman peak FWHMs and the structural properties of the multilayer PtSe<sub>2</sub> films, and also between these structural properties and the film conductivity. Figure 10a plots the E<sub>g</sub> and A<sub>1g</sub> FWHM values of two thick PtSe<sub>2</sub> films synthesized by TAC,<sup>[37]</sup> of our as-grown and annealed MBE films and displays their film conductivities. It also provides key structural information: in-plane domain sizes, SD tilt( $\vec{c}$ ) values, as well as schematics of the domain arrangement within the film thickness. A monocrystalline PtSe<sub>2</sub> sample (> 10 MLs) obtained by mechanical exfoliation is also included as a reference sample.<sup>[43]</sup>

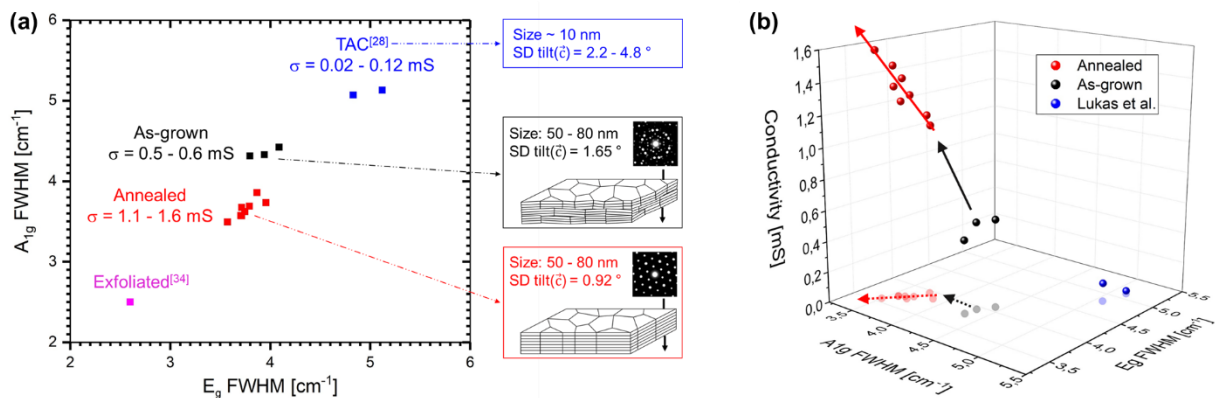


Figure 10. (a) 2D plot for thick (10 - 15 MLs) PtSe<sub>2</sub> films presenting their crystalline quality and conductivity as a function of their Raman peak FWHMs. It displays the E<sub>g</sub> and A<sub>1g</sub> FWHM

values of two PtSe<sub>2</sub>/SiO<sub>2</sub>/Si films synthesized by TAC (blue dots) with thicknesses of 5 and 7.6 nm (10 - 15 MLs range),<sup>[37]</sup> of our as-grown (black dots) and annealed (red dots) PtSe<sub>2</sub>/sapphire(0001) films (12 - 15 MLs) synthesized by MBE under different Se fluxes (0.1 - 0.5 Å.s<sup>-1</sup>) and of the thick (> 10 MLs) exfoliated PtSe<sub>2</sub> sample (purple dot) presenting the lowest reported E<sub>g</sub> and A<sub>1g</sub> FWHM values<sup>[43]</sup> (the conductivity was not reported). It also shows the in-plane domain size and SD tilt( $\vec{c}$ ) values extracted from STEM analyses, and schematics of the domain arrangement within the film thickness with the characteristic diffraction patterns of the MBE films. (b) 3D plot showing the conductivity of the same PtSe<sub>2</sub> samples as a function of E<sub>g</sub> and A<sub>1g</sub> FWHMs. The arrows are guides for the eyes.

First, we investigate the correlations between the E<sub>g</sub> and A<sub>1g</sub> FWHM values and the crystallinity of the samples. It is worth noting that MBE films have much larger in-plane domain sizes and much lower E<sub>g</sub> FWHM compared to TAC films, while all MBE films exhibit similar E<sub>g</sub> FWHM and in-plane domain sizes. This confirms that the E<sub>g</sub> FWHM is well correlated with the in-plane domain size, which is one of the known dominant factors contributing to the in-plane crystalline quality.<sup>[37]</sup> In contrast, the main difference between the annealed and as-grown MBE samples observed by Raman spectroscopy is an important reduction in the A<sub>1g</sub> FWHM for annealed samples. This can be related to the significant improvements in the out-of-plane crystallinity revealed by the in-depth structural analyses in section 2.3, in particular the increase in the domain thickness and the reduction in the out-of-plane tilt disorder (SD tilt( $\vec{c}$ ) of 0.92 ° compared to 1.65 °). The strong reduction in both A<sub>1g</sub> FWHM and SD tilt( $\vec{c}$ ) in as-grown films compared to TAC samples is also consistent with a higher out-of-plane crystallinity. These results suggest that E<sub>g</sub> and A<sub>1g</sub> FWHMs predominantly reflect the in-plane and out-of-plane crystalline quality, respectively. Therefore, these two Raman peak widths need to be investigated together and are relevant metrics to evaluate the overall crystallinity of PtSe<sub>2</sub>. This assumption is supported by the thick (> 10 MLs) PtSe<sub>2</sub> film exfoliated from a single crystal,<sup>[43]</sup> which exhibits significantly lower E<sub>g</sub> and A<sub>1g</sub> FWHM values of 2.6 and 2.5 cm<sup>-1</sup>, respectively. Considering the results obtained in this study, we define a new criterion of high crystalline quality for thick PtSe<sub>2</sub> films ( $\geq 10$  MLs) which is both E<sub>g</sub> and A<sub>1g</sub> FWHMs  $\leq 4$  cm<sup>-1</sup>.

Secondly, we analyze the structural parameters that can influence the film conductivity. As-grown films exhibit higher  $\sigma$  than TAC samples: 0.5 - 0.6 mS compared to 0.02 - 0.12 mS. This can be explained by larger in-plane domain sizes (50 - 80 nm instead of 10 nm) constituting the films, implying a lower GB density. It is interesting to note that not only E<sub>g</sub> FWHM but also

$A_{1g}$  FWHM is smaller for the as-grown films. This suggests the influence of the out-of-plane crystalline quality on the conductivity. For example, the improved film flatness, as evaluated by the SD tilt( $\tilde{c}$ ) values (reduced to 1.65 ° compared to 2.2 - 4.8 °), might be one of the structural parameters that increase the film conductivity. The MBE samples exhibit similar in-plane domain sizes, but the conductivity of annealed films is significantly higher than that of as-grown films (1.1 - 1.6 mS compared to 0.5 - 0.6 mS). This can be explained by their different out-of-plane structural properties, which are monitored by the  $A_{1g}$  FWHM. According to STEM analysis, annealed films consist of a 2D network of vertically single crystalline domains, whereas as-grown films are constituted of a three-dimensional distribution of twisted domains (see schematics in Figure 10a). The domains constituting the annealed films have typically a thickness equal to the film thickness (14 - 15 MLs) and thus, exhibit a metallic behavior.<sup>[14,33,34,36,44]</sup> In contrast, we mainly observed the superposition of 2 to 4 twisted domains within the film thickness of as-grown samples. These domains, which are thinner than the film thickness, can exhibit locally semiconducting behaviors,<sup>[10,12,14,33,34,35,36,39,44]</sup> with various electronic properties depending on their thickness.<sup>[8,29,30]</sup> Therefore, we can assume that as-grown films consist of a mixture of semiconducting and semimetallic phases, as observed in other studies.<sup>[26,37,27]</sup> A much lower local conductivity is expected for the semiconducting phases compared to the semimetallic ones.<sup>[9,33,36,39]</sup> In addition, higher contact resistances are also expected between semiconducting domains with different electronic properties and also between semimetallic and semiconducting domains.<sup>[40]</sup> Therefore, achieving the domain thickness equal to the film thickness is particularly important for high film conductivity. Annealed films, which satisfies this criterion, exhibit record conductivities for grown films. If this condition is not satisfied, the film conductivity strongly depends on the thickness of component domains. Note that Figure 1b which plots the conductivity of only as-grown films (with unknown domain thickness) as a function of the film thickness is therefore highly complex to interpret. This observation may also explain the large variation in the number of layers, reported in different works,<sup>[10,14,30,33,34,35,36]</sup> at which the semiconducting-to-metallic transition occurs. For an accurate determination of the layer number for this transition, it is essential to ensure that the PtSe<sub>2</sub> films consist of vertically aligned single crystalline domains.<sup>[30]</sup> It is also interesting to note that the impact of the post-growth annealing on the PtSe<sub>2</sub> conductivity might arise from an original mechanism: indeed, in conventional materials, the increase in crystallinity reduces carrier scattering, thereby increasing electronic mobility and conductivity. In contrast, in multilayer PtSe<sub>2</sub>, the increased out-of-plane crystallinity can

also change the nature of the material itself, by affecting its local electronic structures, turning it from a semiconductor to a semimetal.

Figure 10b plots in 3D the conductivity of the same samples as a function of both the  $E_g$  and  $A_{1g}$  FWHM values. It clearly shows the correlation between crystallinity and conductivity: films with lower  $E_g$  and  $A_{1g}$  FWHMs exhibit higher conductivities. Previous studies on PtSe<sub>2</sub> films only considered the  $E_g$  FWHM as an indicator of crystallinity and conductivity. Here, we show that the Raman peak widths become robust metrics when both the in-plane  $E_g$  mode and the out-of-plane  $A_{1g}$  mode are investigated together. This approach allows the perception of various types of structural changes and provides a fast and reliable evaluation of film quality in terms of both structural and electrical properties. Our study suggests a correlation between the  $E_g$  FWHM and in-plane crystalline quality, and between the  $A_{1g}$  FWHM and out-of-plane crystalline quality. Studying the increase in conductivity in conjunction with the evolutions of  $E_g$  and  $A_{1g}$  FWHMs provides insight into the type of responsible structural evolution. For example, the significant improvement in the out-of-plane crystalline quality induced by the post-growth annealing is efficiently identified by the significant reduction in the  $A_{1g}$  FWHM (black dashed arrow), and is mainly responsible for the increased conductivity observed between as-grown and annealed samples (black arrow). For annealed films, a linear dependence of the film conductivity on both the  $E_g$  and  $A_{1g}$  FWHM values is clearly visible in this plot (red arrow) and in Figure 4(b-c). The high correlation between these two metrics and the conductivity demonstrates the effectiveness of such a plot in monitoring the synthesis process. For these annealed films, it is mainly the increase in the Se flux used during syntheses that is at the origin of the decrease in the  $E_g$  and  $A_{1g}$  FWHMs, and consequently of the increase in the conductivity.

Our best MBE film exhibits low  $E_g$  and  $A_{1g}$  FWHMs of 3.6 and 3.5  $\text{cm}^{-1}$ , respectively, inducing a record conductivity of 1.6 mS for grown PtSe<sub>2</sub> films. As the lowest  $E_g$  and  $A_{1g}$  FWHM values reported for an exfoliated film are close to 2.5  $\text{cm}^{-1}$  for both peaks,<sup>[43]</sup> this plot highlights that the conductivity of grown PtSe<sub>2</sub> films can be still improved and that the intrinsic transport properties of PtSe<sub>2</sub> remain to be determined.

In summary, this study successfully demonstrates the relevance and efficiency of using  $E_g$  and  $A_{1g}$  FWHMs as new Raman metrics for evaluating the film quality in terms of both structural and electrical properties. These metrics also offer valuable insights into the underlying mechanisms, highlighting their utility for monitoring the synthesis process.

## 2.5. Photodetection and optoelectronic mixing at 1.55 $\mu\text{m}$

We fabricated both DC and RF devices to measure the electrical conductivity of PtSe<sub>2</sub> channels integrated into devices and to demonstrate high-frequency photodetectors and OEMs operating at the 1.55  $\mu\text{m}$  telecom wavelength. First, a 14ML PtSe<sub>2</sub> film was synthesized directly on a 2-inch sapphire(0001) substrate. When the device fabrication started, the synthesis study was still in progress and we selected the following conditions:  $T_g = 520\text{ }^\circ\text{C}$  and  $T_a = 690\text{ }^\circ\text{C}$  under  $0.3\text{ }\text{\AA}\cdot\text{s}^{-1}$  of Se. Note that these conditions are not optimal, as the synthesis was not performed under a Se flux of  $0.5\text{ }\text{\AA}\cdot\text{s}^{-1}$  (see section 2.2), but a film composed of only semimetallic domains is still expected, as demonstrated in section 2.4. The fabrication process (detailed in Figure S13) includes a first lithographic and etching step to define the different PtSe<sub>2</sub> channels and then, a two-step process to contact the channel edges and define the metallic pads. Figure 11a shows the 2-inch sapphire substrate integrating an array of identical cells: measurements were performed on all the devices in the 9 central cells. Each cell contains DC and RF devices. We first characterized the DC devices (Figure 11b) integrating a  $20 \times 5.4\text{ }\mu\text{m}^2$  PtSe<sub>2</sub> channel (length and width, respectively, are measured at the end of the fabrication process). Using the four-contact measurement method at room temperature on 378 devices from different cells, we obtain a median value of  $R_{\square} = 0.95\text{ k}\Omega\cdot\text{\AA}^{-1}$  (corresponding to  $\sigma = 1.06\text{ mS}$ ) with a standard deviation of  $0.19\text{ k}\Omega\cdot\text{\AA}^{-1}$  (see Figure S14). The measured conductivity is close to that obtained on the  $20 \times 20\text{ mm}^2$  samples, i.e.  $1.13 - 1.31\text{ mS}$  (for a Se flux of  $0.3\text{ }\text{\AA}\cdot\text{s}^{-1}$ ), indicating that the high quality of the PtSe<sub>2</sub> film synthesized on a 2-inch substrate is maintained after device fabrication. The contact resistance of the devices obtained by the four-contact method is below the measurement precision ( $< 100\text{ }\Omega\cdot\mu\text{m}$ ), such a low value is characteristic of semimetallic PtSe<sub>2</sub> films.<sup>[33,40]</sup>

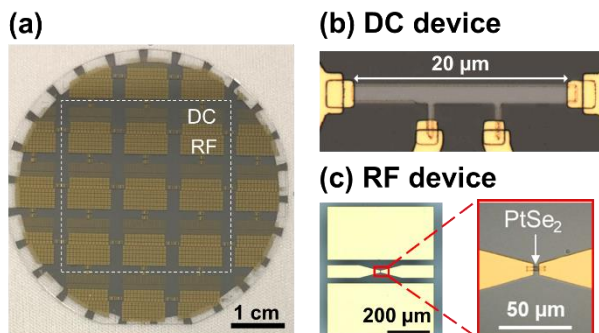


Figure 11. (a) PtSe<sub>2</sub>-based devices on a 2-inch sapphire substrate. Each cell is identical and integrates DC and RF devices. Measurements were performed on all the devices within the



white square. (b) Optical image of a four-contact DC device used to measure the sheet and contact resistance of the PtSe<sub>2</sub> channel. (c) Optical image of a 3.5 x 3 μm<sup>2</sup> PtSe<sub>2</sub> channel integrated into the signal line of a CPW. These devices are used for high-frequency photodetection and mixing.

High-frequency optoelectronic measurements (detailed in Figure S15) are performed at room temperature with coplanar waveguides (CPWs) integrating a 3.5 x 3 μm<sup>2</sup> PtSe<sub>2</sub> channel (RF device in Figure 11c). We first characterized these devices as photodetectors (Figure 12a). As our PtSe<sub>2</sub> channel acts as a photoconductor, a DC bias ( $V_{DC} = 4$  V) is applied to it. The channel is also illuminated by a 1.55 μm laser whose intensity is modulated with a Mach-Zehnder device at frequencies  $f_{opt}$  varying between 2 and 67 GHz. The photodetected power ( $P_{ph}$ ) is measured as a function of  $f_{opt}$  for optical powers ( $P_{opt}$ ) ranging between 14.2 and 41.5 mW. The modulation efficiency of the channel resistance increases with the optical power, resulting in an increase in the photodetected power. Figure 12b shows a flat photodetected signal with a responsivity of around 0.2 mA.W<sup>-1</sup> (~ 8.5 μA at 41.5 mW) and a record cutoff frequency (at -3 dB) of 60 GHz. Ji et al.<sup>[13]</sup> investigated the carrier dynamics in our photoexcited thick PtSe<sub>2</sub> films using optical-pump THz probe spectroscopy. An ultrafast photoresponse of 1.4 ps was measured for a pump light at a wavelength of 400 nm, meaning that the cutoff frequency observed in our photodetection measurements might be limited by the photocarrier lifetime.

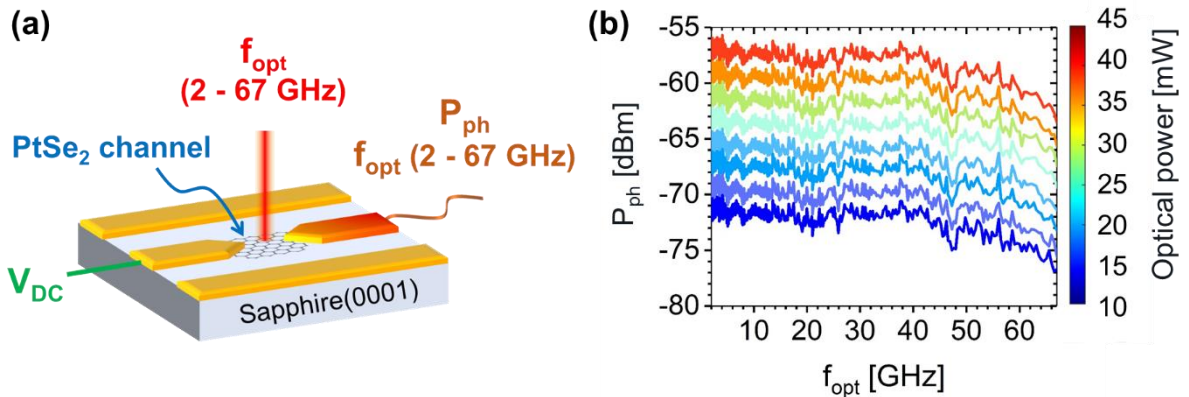


Figure 12. (a) Schematic of the photodetection measurements: CPW integrates a 3.5 x 3 μm<sup>2</sup> PtSe<sub>2</sub> channel. A DC bias ( $V_{DC} = 4$  V) is applied to the input signal line. A 1.55 μm laser spot, with a diameter of 2.5 μm, is focused on the PtSe<sub>2</sub> channel. The laser power is modulated at a

frequency ( $f_{\text{opt}}$ ) varying between 2 and 67 GHz. (c) Photodetected power ( $P_{\text{ph}}$ ) measured as a function of  $f_{\text{opt}}$  for different optical powers.

Optoelectronic mixing experiments (detailed in Figure S15) are also performed on the same RF devices. This device is able to mix the input RF signal and the optical power because the output signal depends on both the optical power and the channel bias, as shown in Figure 13a. When operating as an OEM, the PtSe<sub>2</sub> channel bias is provided by the input RF signal. A RF signal with a power  $P_{\text{RF}} = -10$  dBm and at frequency  $f_{\text{RF}}$  varying between 0.01 and 29.99 GHz is injected into the PtSe<sub>2</sub> CPW (Figure 13b). The laser power and the modulation frequency are fixed at  $P_{\text{opt}} = 60$  mW and  $f_{\text{opt}} = 30$  GHz, respectively. The output power ( $P_{\text{IF}}$ ) is measured at the intermediate frequency  $f_{\text{IF}} = f_{\text{opt}} - f_{\text{RF}}$ , which also varies between 0.01 and 29.99 GHz. Figure 13c shows the conversion efficiency, which is the  $P_{\text{IF}}/P_{\text{RF}}$  ratio. This efficiency is constant over the whole frequency range, which proves a bandwidth above 30 GHz, and reaches -73 dB. This value is 10 dB better than the value obtained by Montanaro et al.<sup>[46]</sup> with graphene CPWs fabricated on a 2-inch SiO<sub>2</sub>/Si substrate and highlights the potential of PtSe<sub>2</sub> for high-frequency optoelectronics.

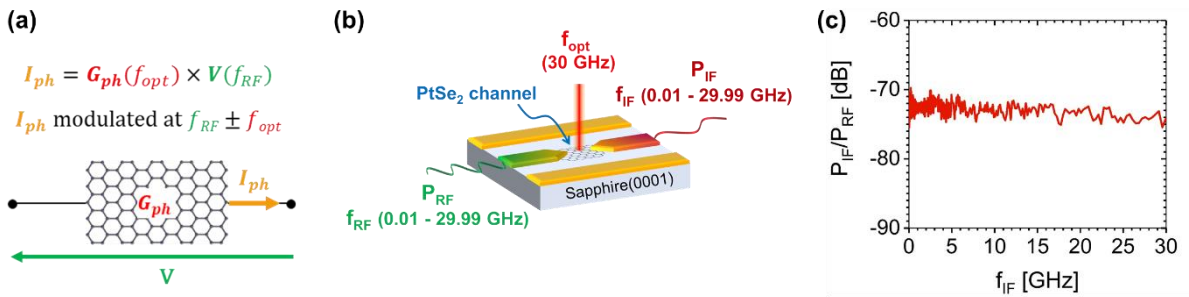


Figure 13. (a) Schematic of the optoelectronic mixing mechanism. The output photocurrent ( $I_{\text{ph}}$ ) depends both on the voltage ( $V$ , modulated at  $f_{\text{RF}}$ ) applied on the PtSe<sub>2</sub> channel and on the photoconductance ( $G_{\text{ph}}$ , modulated at  $f_{\text{opt}}$ ). The output signal includes a signal modulated at  $f_{\text{RF}} + f_{\text{opt}}$  and another one at  $f_{\text{RF}} - f_{\text{opt}}$ . (b) Schematic of the optoelectronic mixing experiments. A 1.55  $\mu\text{m}$  laser spot, with a diameter of 2.5  $\mu\text{m}$ , is focused on the PtSe<sub>2</sub> channel. The laser power is modulated at a fixed frequency ( $f_{\text{opt}}$ ) of 30 GHz. The input RF signal is modulated at a frequency  $f_{\text{RF}}$  varying between 0.01 and 29.99 GHz. The output power  $P_{\text{IF}}$  is measured at the intermediate frequency  $f_{\text{IF}} = f_{\text{opt}} - f_{\text{RF}}$  varying between 0.01 and 29.99 GHz. (c) Conversion efficiency ( $P_{\text{IF}}/P_{\text{RF}}$ ) as a function of  $f_{\text{IF}}$ .

### 3. Conclusion

Raman spectroscopy is a fast and robust technique to optimize the synthesis of PtSe<sub>2</sub> multilayers, but it requires the study of the A<sub>1g</sub> FWHM in addition to the commonly used E<sub>g</sub> FWHM. Indeed, our study has shown that both E<sub>g</sub> and A<sub>1g</sub> FWHMs are effective metrics for assessing the crystalline quality and film conductivity of PtSe<sub>2</sub> multilayers. Moreover, performing a 3D plot of the film conductivity as a function of both E<sub>g</sub> and A<sub>1g</sub> FWHMs is particularly useful to monitor the synthesis: the lower the E<sub>g</sub> and A<sub>1g</sub> FWHM, the higher the overall crystallinity and conductivity of the films. Investigating E<sub>g</sub> and A<sub>1g</sub> peaks together encompasses both in-plane and out-of-plane structural factors. The analysis of these Raman metrics applied to our MBE samples, but also to films synthesized by TAC, suggests that E<sub>g</sub> and A<sub>1g</sub> FWHMs predominantly reflect the in-plane and out-of-plane crystalline quality, respectively.

Concerning the MBE synthesis of thick (12 - 16 MLs) PtSe<sub>2</sub> films on sapphire(0001), we have shown that a high growth temperature (520 °C) combined with a high Se flux (0.1 - 0.5 A.s<sup>-1</sup>) results in films exhibiting very low E<sub>g</sub> FWHM values ( $\leq 4 \text{ cm}^{-1}$ ) but a limited electrical conductivity (0.5 - 0.6 mS). Performing a post-growth annealing step at 690 °C under these high Se fluxes allows obtaining samples with a high crystalline quality in both the in-plane and out-of-plane directions (exhibiting both E<sub>g</sub> and A<sub>1g</sub> FWHMs  $\leq 4 \text{ cm}^{-1}$ ), resulting in record conductivities for grown PtSe<sub>2</sub> (1.1 - 1.6 mS). The lowest values of both FWHMs and conductivity are obtained for the highest Se flux of 0.5 A.s<sup>-1</sup>, which emphasizes the importance of this high  $\Phi(\text{Se})/\Phi(\text{Pt})$  ratio over the synthesis process. In-depth XRD and STEM analyses have revealed that this post-growth annealing induces remarkable structural evolutions responsible for significant improvements in the out-of-plane crystallinity, which are monitored by the strong reduction in A<sub>1g</sub> FWHM. In-plane defect diffusion and GB migration are induced by the annealing under high Se flux, enhancing the local in-plane layer quality, which may explain the slight decrease in E<sub>g</sub> FWHM. This in-plane crystal reorganization, in turn, leads to an improvement in the out-of-plane crystalline quality across the entire volume of films, due to the enhancement in interlayer binding energy.

This work also shown the crucial importance of monitoring the domain thickness in the case of PtSe<sub>2</sub> to control its electronic properties. For example, our annealed samples (with E<sub>g</sub> and A<sub>1g</sub> FWHMs  $\leq 4 \text{ cm}^{-1}$ ) exhibit a 2D network of vertically single crystalline domains with domain thickness corresponding to the film thickness and present record conductivities. In contrast, when the domain thickness is less than the film thickness (e.g. our as-grown samples with A<sub>1g</sub>

FWHM  $> 4 \text{ cm}^{-1}$ ), the film conductivity depends not only on the film thickness but also on the thickness of component domains. Therefore, it is essential to perform a post-growth annealing to achieve domain thickness equal to the film thickness and obtain high conductivity films. Our best 15 ML MBE film exhibits very low  $E_g$  and  $A_{1g}$  FWHMs of 3.6 and 3.5  $\text{cm}^{-1}$  respectively, inducing a record conductivity of 1.6 mS compared to the state of the art ( $\leq 0.3$  mS for grown films). This record value is equal to the best value reported for a 16 ML exfoliated PtSe<sub>2</sub>. Very recently,  $E_g$  and  $A_{1g}$  FWHM values as low as  $\sim 2.5 \text{ cm}^{-1}$  have been demonstrated with an exfoliated film, indicating that the crystalline quality, and consequently the conductivity, of MBE PtSe<sub>2</sub> films can still be improved. To reach this goal, research efforts could focus on improving the layer quality, for instance by reducing the GB density through epitaxial growth methods. An example is the recently reported growth of MoS<sub>2</sub> on a sapphire vicinal surface, which achieved a 99 % alignment of the in-plane orientations across different domains.<sup>[67,68,69]</sup> Such a method applied to PtSe<sub>2</sub> should produce epitaxial films with a significant reduction in GB density and a higher conductivity.

Finally, high quality semimetallic PtSe<sub>2</sub> films have been synthesized on a 2-inch sapphire substrate to fabricate optoelectronic devices operating at the telecom wavelength of 1.55  $\mu\text{m}$ . We have presented photodetectors with a record bandwidth of 60 GHz and the first 30GHz-bandwidth optoelectronic mixer based on a TMD film. Considering these results and the exceptional air stability observed over 1.5 years with preserved electrical properties, PtSe<sub>2</sub> is a very promising material for high-frequency IR optoelectronics.

#### 4. Methods

*PtSe<sub>2</sub> synthesis:* the growth reactor is a 2-inch MBE system supplied by Dr Eberl MBE-Komponenten. PtSe<sub>2</sub> is synthesized on c-plane (0001) sapphire surfaces purchased from Kyocera Corporation (Japan). 20 x 20  $\text{mm}^2$  samples are implemented for growth studies (Sections 2.1 to 2.4), and a 2-inch substrate was used to demonstrate photodetection and optoelectronic mixing (Section 2.5). The substrates are first chemically cleaned with acetone/propanol and a 100nm-thick Mo film is deposited on the back to improve the radiative heating of the substrate in the growth chamber. The substrates are outgassed under ultra-high vacuum ( $10^{-10}$  mbar) at 500 °C overnight and then, annealed at 900 °C during 15 min. A valved selenium cracker source is used: the tank filled with ultra-high purity (7N) Se is heated to 290 °C and the cracker temperature is maintained at 600 °C. The electron beam evaporator generates a

Pt flux from high purity (4N) Pt. Se and Pt fluxes are calibrated prior to synthesis using a quartz crystal microbalance positioned at the sample position. The growth and annealing temperatures listed in the article correspond to the values provided by the thermocouple located behind the sample.

*Raman spectroscopy:* the Raman spectroscope Labram HR Evolution from Horiba is used at room temperature with a 532 nm laser excitation, a laser power of 0.25 mW and a grating of 1800 grooves.mm<sup>-1</sup>. Raman spectra were acquired at 9 positions evenly distributed on each 20 x 20 mm<sup>2</sup> sample to extract the median value of the E<sub>g</sub> FWHM and A<sub>1g</sub> FWHM plotted in Figures 2 and 3. The plotted vertical lines indicate the first and third quartile of the 9 FWHM values and characterize the inhomogeneity of the PtSe<sub>2</sub> films. The A<sub>1g</sub> FWHM values present larger interquartile values compared to the E<sub>g</sub> FWHM due to the lower signal-to-noise ratio of the A<sub>1g</sub> peak.

*EDX measurements:* the ZEISS SIGMA SEM is used with an acceleration voltage of 5 kV, on a scan area of 20 x 20 μm<sup>2</sup> at two different positions for each sample.

*XRD measurements:* we implement a Rigaku Smartlab diffractometer equipped with a high brilliance rotating anode and a 5-circle goniometer. In-plane GIXRD measurements are performed without monochromator, with a double tilt wafer stage to maintain a fixed grazing incidence geometry during the sample rotation. The grazing angle is 0.4 °, resulting in an illuminated area of ~ 1 cm<sup>2</sup>. Incident and diffracted beam parallel slit collimators are used to define a 0.5 ° angular resolution. A Ge(220) 2-bounce monochromator is used for out-of-plane HRXRD measurements. The PtSe<sub>2</sub> diffraction peaks are indexed using the file ICDD 03-065-3374, which corresponds to a hexagonal structure with a space group P-3m1 (164).

*STEM imaging:* PtSe<sub>2</sub> films are transferred to a TEM grid to perform STEM plane views. First, a 100nm-thick Au layer is evaporated on PtSe<sub>2</sub>. The Au/PtSe<sub>2</sub> stack is peeled off with a standard dicing tape and deposited onto a clean Si/SiO<sub>2</sub> wafer. The Au layer is cleaned and then etched with a KI<sub>2</sub> solution. The PtSe<sub>2</sub> film is picked up with a stamp made of a polypropylene carbonate (PPC) layer spin-coated on a polydimethylsiloxane (PDMS) droplet and released at 120 °C on the TEM grid. It is finally cleaned in acetone/isopropanol to remove polymer residues. STEM analysis are performed using probe aberration corrected microscopes, Titan Themis (Thermofisher) and Titan Ultimate (Thermofisher), operating at 200 kV. The 4D-datasets are obtained using a direct electron detector (Quantum Detector, Medipix-Merlin) equipped in Titan Ultimate, in single pixel continuous mode with a T0 threshold of 30 keV, a convergence angle of 1 mrad and probe size of 1 nm.

*Conductivity measurements:* after PtSe<sub>2</sub> synthesis, Ti(20 nm)/Au(400 nm) pads of 1.2 mm diameter are evaporated through a shadow mask at each corner of the 18.5 x 18.5 mm<sup>2</sup> PtSe<sub>2</sub> films grown on the 20 x 20 mm<sup>2</sup> substrates. Conductivity measurements are then performed using a Hall-effect measurement bench Ecopia HMS 7000 with a current of 1 mA.

### **Acknowledgements**

The authors acknowledge the financial support from the European Union's Horizon 2020 program under grant agreement no. 881603 (Core3 Graphene Flagship), as well as from ANR-2018-CE08-018-05 (BIRDS) and ANR-20-CE09-0026 (2DonDemand).

H. Okuno and D. Dosenovic acknowledge financial support from the European Union's H2020 Research and Innovation program via the e-See project (Grant No. 758385).

The authors also acknowledge the French RENATECH network for its financial support

The authors also acknowledge Stepan Shvarkov from MBE-Komponenten and Laurent Travers from C2N for their great support and advise to implement the MBE reactor.

## References

---

- <sup>1</sup> T. Tan, X. Jiang, C. Wang, B. Yao, H. Zhang, *Advanced Science* **2020**, 7, 2000058.
- <sup>2</sup> J. Zha, M. Luo, M. Ye, T. Ahmed, X. Yu, D. Lien, Q. He, D. Lei, J. C. Ho, J. Bullock, K. B. Crozier, C. Tan, *Adv Funct Materials* **2022**, 32, 2111970.
- <sup>3</sup> J. You, Y. Luo, J. Yang, J. Zhang, K. Yin, K. Wei, X. Zheng, T. Jiang, *Laser & Photonics Reviews* **2020**, 14, 2000239.
- <sup>4</sup> X. Wang, Y. Cui, T. Li, M. Lei, J. Li, Z. Wei, *Advanced Optical Materials* **2018**, 7, 1801274.
- <sup>5</sup> A. Quellmalz, X. Wang, S. Sawallich, B. Uzlu, M. Otto, S. Wagner, Z. Wang, M. Prechtel, O. Hartwig, S. Luo, G. S. Duesberg, M. C. Lemme, K. B. Gylfason, N. Roxhed, G. Stemme, F. Niklaus, *Nat Commun* **2021**, 12, 917.
- <sup>6</sup> A. J. Watson, W. Lu, M. H. D. Guimarães, M. Stöhr, *2D Mater.* **2021**, 8, 032001.
- <sup>7</sup> D. Akinwande, C. Huyghebaert, C.-H. Wang, M. I. Serna, S. Goossens, L.-J. Li, H.-S. P. Wong, F. H. L. Koppens, *Nature* **2019**, 573, 507.
- <sup>8</sup> Z. Huang, W. Zhang, W. Zhang, *Materials* **2016**, 9, 716.
- <sup>9</sup> Y. Zhao, J. Qiao, Z. Yu, P. Yu, K. Xu, S. P. Lau, W. Zhou, Z. Liu, X. Wang, W. Ji, Y. Chai, *Advanced Materials* **2017**, 29, 1604230.
- <sup>10</sup> Y. Yang, S. K. Jang, H. Choi, J. Xu, S. Lee, *Nanoscale* **2019**, 11, 21068.
- <sup>11</sup> S. S. Han, J. H. Kim, C. Noh, J. H. Kim, E. Ji, J. Kwon, S. M. Yu, T.-J. Ko, E. Okogbue, K. H. Oh, H.-S. Chung, Y. Jung, G.-H. Lee, Y. Jung, *ACS Appl. Mater. Interfaces* **2019**, 11, 13598.
- <sup>12</sup> F. Bonell, A. Marty, C. Vergnaud, V. Consonni, H. Okuno, A. Ouerghi, H. Boukari, M. Jamet, *2D Mater.* **2022**, 9, 015015.
- <sup>13</sup> J. Ji, Y. Zhou, B. Zhou, E. Desgué, P. Legagneux, P. U. Jepsen, P. Bøggild, *ACS Appl. Mater. Interfaces* **2023**, 15, 51319.
- <sup>14</sup> X. Yu, P. Yu, D. Wu, B. Singh, Q. Zeng, H. Lin, W. Zhou, J. Lin, K. Suenaga, Z. Liu, Q. J. Wang, *Nat Commun* **2018**, 9, 1545.
- <sup>15</sup> K. Zhang, M. Feng, Y. Ren, F. Liu, X. Chen, J. Yang, X.-Q. Yan, F. Song, J. Tian, *Photon. Res.* **2018**, 6, 893.
- <sup>16</sup> G. Wang, Z. Wang, N. McEvoy, P. Fan, W. J. Blau, *Advanced Materials* **2021**, 33, 2004070.
- <sup>17</sup> C. Yim, N. McEvoy, S. Riazimehr, D. S. Schneider, F. Gity, S. Monaghan, P. K. Hurley, M. C. Lemme, G. S. Duesberg, *Nano Letters* **2018**, 18, 1794.
- <sup>18</sup> S. Parhizkar, M. Prechtel, A. L. Giesecke, S. Suckow, S. Wahl, S. Lukas, O. Hartwig, N. Negm, A. Quellmalz, K. Gylfason, D. Schall, M. Wuttig, G. S. Duesberg, M. C. Lemme, *ACS Photonics* **2022**, 9, 859.

- 
- <sup>19</sup> Y. Wang, Z. Yu, Y. Tong, B. Sun, Z. Zhang, J.-B. Xu, X. Sun, H. K. Tsang, *Applied Physics Letters* **2020**, *116*, 211101.
- <sup>20</sup> Y. Wang, Z. Yu, Z. Zhang, B. Sun, Y. Tong, J.-B. Xu, X. Sun, H. K. Tsang, *ACS Photonics* **2020**, *7*, 2643.
- <sup>21</sup> Z. Tang, Y. Li, J. Yao, S. Pan, *Laser & Photonics Reviews* **2020**, *14*, 1800350.
- <sup>22</sup> A. Montanaro, S. Mzali, J.-P. Mazellier, O. Bezencenet, C. Larat, S. Molin, L. Morvan, P. Legagneux, D. Dolfi, B. Dlubak, P. Seneor, M.-B. Martin, S. Hofmann, J. Robertson, A. Centeno, A. Zurutuza, *Nano Lett.* **2016**, *16*, 2988.
- <sup>23</sup> A. Montanaro, W. Wei, D. De Fazio, U. Sassi, G. Soavi, P. Aversa, A. C. Ferrari, H. Happy, P. Legagneux, E. Pallecchi, *Nat Commun* **2021**, *12*, 2728.
- <sup>24</sup> L. Hamidouche, A. Montanaro, M. Rosticher, E. Grimaldi, B. Poupet, T. Taniguchi, K. Watanabe, B. Plaçais, E. Baudin, P. Legagneux, *ACS Photonics* **2021**, *8*, 369.
- <sup>25</sup> M. Tharrault, E. Grimaldi, D. Pommier, L. Hamidouche, P. Berger, S. Combrie, G. Baili, M. Rostischer, T. Taniguchi, K. Watanabe, B. Plaçais, E. Baudin, P. Legagneux, *Adv Elect Materials* **2023**, *9*, 2300260.
- <sup>26</sup> X. Zhao, F. Liu, D. Liu, X.-Q. Yan, C. Huo, W. Hui, J. Xie, Q. Ye, C. Guo, Y. Yao, Z.-B. Liu, J.-G. Tian, *Applied Physics Letters* **2019**, *115*, 263102.
- <sup>27</sup> J. Xie, D. Zhang, X.-Q. Yan, M. Ren, X. Zhao, F. Liu, R. Sun, X. Li, Z. Li, S. Chen, Z.-B. Liu, J.-G. Tian, *2D Materials* **2019**, *6*, 035011.
- <sup>28</sup> F. Liu, P. Li, H. An, P. Peng, B. McLean, F. Ding, *Adv Funct Materials* **2022**, *32*, 2203191.
- <sup>29</sup> A. Kandemir, B. Akbali, Z. Kahraman, S. V. Badalov, M. Ozcan, F. Iyikanat, H. Sahin, *Semicond. Sci. Technol.* **2018**, *33*, 085002.
- <sup>30</sup> M. Tharrault, S. Ayari, M. Arfaoui, E. Desgué, R. L. Goff, P. Morfin, J. Palomo, M. Rosticher, S. Jaziri, B. Plaçais, P. Legagneux, F. Carosella, C. Voisin, R. Ferreira, E. Baudin, *Phys. Rev. Lett.* **2025**, *134*, 066901.
- <sup>31</sup> L. Zhang, T. Yang, M. F. Sahdan, Arramel, W. Xu, K. Xing, Y. P. Feng, W. Zhang, Z. Wang, A. T. S. Wee, *Adv Elect Materials* **2021**, *7*, 2100559.
- <sup>32</sup> J. Li, S. Kolekar, M. Ghorbani-Asl, T. Lehnert, J. Biskupek, U. Kaiser, A. V. Krashenninnikov, M. Batzill, *ACS Nano* **2021**, *15*, 13249.
- <sup>33</sup> A. Ciarrocchi, A. Avsar, D. Ovchinnikov, A. Kis, *Nat Commun* **2018**, *9*, 919.
- <sup>34</sup> T. Su, H. Medina, Y. Chen, S. Wang, S. Lee, Y. Shih, C. Chen, H. Kuo, F. Chuang, Y. Chueh, *Small* **2018**, *14*, 1800032.
- <sup>35</sup> K. Xiong, M. Hilse, L. Li, A. Goritz, M. Lisker, M. Wietstruck, M. Kaynak, R. Engel-Herbert, A. Madjar, J. C. M. Hwang, *IEEE Transaction on Electron Devices* **2020**, *67*, 796.



- 
- <sup>36</sup> W. Jiang, X. Wang, Y. Chen, G. Wu, K. Ba, N. Xuan, Y. Sun, P. Gong, J. Bao, H. Shen, T. Lin, X. Meng, J. Wang, Z. Sun, *InfoMat* **2019**, 1, 260.
- <sup>37</sup> S. Lukas, O. Hartwig, M. Prechtel, G. Capraro, J. Bolten, A. Meledin, J. Mayer, D. Neumaier, S. Kataria, G. S. Duesberg, M. C. Lemme, *Adv Funct Materials* **2021**, 31, 2102929.
- <sup>38</sup> R. Kempt, S. Lukas, O. Hartwig, M. Prechtel, A. Kuc, T. Brumme, S. Li, D. Neumaier, M. C. Lemme, G. S. Duesberg, T. Heine, *Advanced Science* **2022**, 9, 2201272.
- <sup>39</sup> M. A. Aslam, S. Leitner, S. Tyagi, A. Provias, V. Tkachuk, E. Pavlica, M. Dienstleder, D. Knez, K. Watanabe, T. Taniguchi, D. Yan, Y. Shi, T. Knobloch, M. Walzl, U. Schwingenschlögl, T. Grasser, A. Matković, *Nano Letters* **2024**, 24, 6529.
- <sup>40</sup> B. M. Szydłowska, O. Hartwig, B. Tywoniuk, T. Hartman, T. Stimpel-Lindner, Z. Sofer, N. McEvoy, G. S. Duesberg, C. Backes, *2D Mater.* **2020**, 7, 045027.
- <sup>41</sup> T. Das, E. Yang, J. E. Seo, J. H. Kim, E. Park, M. Kim, D. Seo, J. Y. Kwak, J. Chang, *ACS Appl. Mater. Interfaces* **2021**, 13, 1861.
- <sup>42</sup> S. Bae, S. Nah, D. Lee, M. Sajjad, N. Singh, K. M. Kang, S. Kim, G. Kim, J. Kim, H. Baik, K. Lee, S. Sim, *Small* **2021**, 17, 2103400.
- <sup>43</sup> M. Tharrault, E. Desgué, D. Carisetti, B. Plaçais, C. Voisin, P. Legagneux, E. Baudin, *2D Mater.* **2024**, 11, 025011.
- <sup>44</sup> H. Xu, H. Zhang, Y. Liu, S. Zhang, Y. Sun, Z. Guo, Y. Sheng, X. Wang, C. Luo, X. Wu, J. Wang, W. Hu, Z. Xu, Q. Sun, P. Zhou, J. Shi, Z. Sun, D. W. Zhang, W. Bao, *Adv Funct Materials* **2019**, 29, 1805614.
- <sup>45</sup> M. O'Brien, N. McEvoy, C. Motta, J.-Y. Zheng, N. C. Berner, J. Kotakoski, K. Elibol, T. J. Pennycook, J. C. Meyer, C. Yim, M. Abid, T. Hallam, J. F. Donegan, S. Sanvito, G. S. Duesberg, *2D Mater.* **2016**, 3, 021004.
- <sup>46</sup> L. Li, K. Xiong, R. J. Marstell, A. Madjar, N. C. Strandwitz, J. C. M. Hwang, N. McEvoy, J. B. McManus, G. S. Duesberg, A. Goritz, M. Wietstruck, M. Kaynak, *IEEE Transactions On Electron Devices* **2018**, 65, 4102.
- <sup>47</sup> Y. Wang, L. Li, W. Yao, S. Song, J. T. Sun, J. Pan, X. Ren, C. Li, E. Okunishi, Y.-Q. Wang, E. Wang, Y. Shao, Y. Y. Zhang, H. Yang, E. F. Schwier, H. Iwasawa, K. Shimada, M. Taniguchi, Z. Cheng, S. Zhou, S. Du, S. J. Pennycook, S. T. Pantelides, H.-J. Gao, *Nano Lett.* **2015**, 15, 4013.
- <sup>48</sup> M. Hilse, K. Wang, R. Engel-Herbert, *2D Mater.* **2020**, 7, 045013.

- 
- <sup>49</sup> M. Yan, E. Wang, X. Zhou, G. Zhang, H. Zhang, K. Zhang, W. Yao, N. Lu, S. Yang, S. Wu, T. Yoshikawa, K. Miyamoto, T. Okuda, Y. Wu, P. Yu, W. Duan, S. Zhou, *2D Mater.* **2017**, *4*, 045015.
- <sup>50</sup> M. Hilse, K. Wang, R. Engel-Herbert, *2D Mater.* **2022**, *9*, 025029.
- <sup>51</sup> Y. Li, T. F. Heinz, *2D Mater.* **2018**, *5*, 025021.
- <sup>52</sup> D. S. H. Liu, M. Hilse and R. Engel-Herbert, *J. Vac. Sci. Technol. A* **2021**, *39*, 023413
- <sup>53</sup> Y. Tong, M. Bouaziz, H. Oughaddou, H. Enriquez, K. Chaouchi, F. Nicolas, S. Kubsky, V. Esaulov, A. Bendounan, *RSC Adv.* **2020**, *10*, 30934.
- <sup>54</sup> K. Zhang, M. Yan, H. Zhang, H. Huang, M. Arita, Z. Sun, W. Duan, Y. Wu, S. Zhou, *Physical Review. B.* **2017**, *96*, 125102.
- <sup>55</sup> G. K. Williamson, W. H. Hall, *Acta Metallurgica* **1953**, *1*, 22.
- <sup>56</sup> S. Dolabella, A. Borzì, A. Dommann, A. Neels, *Small Methods* **2021**, *6*, 2100932.
- <sup>57</sup> M. J. Hÿtch, E. Snoeck, R. Kilaas, *Ultramicroscopy* **1998**, *74*, 131.
- <sup>58</sup> J. L. Rouvière, E. Sarigiannidou, *Ultramicroscopy* **2005**, *106*, 1.
- <sup>59</sup> D. Ke, J. Hong, Y. Zhang, *Nanoscale Advances* **2023**, *5*, 2657.
- <sup>60</sup> C. J. Alvarez, M. T. Dau, A. Marty, C. Vergnaud, H. Le Poche, P. Pochet, M. Jamet and H. Okuno, *Nanotechnology* **2018**, *29*, 425706.
- <sup>61</sup> A. V. Tyurnina, H. Okuno, P. Pochet and J. Dijon, *Carbon* **2016**, *102*, 499.
- <sup>62</sup> X. Liu, Z. G. Yu, G. Zhang, Y.-W. Zhang, *Nanoscale* **2020**, *12*, 17746.
- <sup>63</sup> X. Zhao, Y. Ji, J. Chen, W. Fu, J. Dan, Y. Liu, S. J. Pennycook, W. Zhou, K. P. Loh, *Advanced Materials* **2019**, *31*, 1900237.
- <sup>64</sup> Y. Zhang, J.-H. Baek, C.-H. Lee, Y. Jung, S. C. Hong, G. Nolan, K. Watanabe, T. Taniguchi, G.-H. Lee, P. Y. Huang, *Science Advances* **2024**, *10*.
- <sup>65</sup> A. Azizi, X. Zou, P. Ercius, Z. Zhang, A. L. Elías, N. Perea-López, G. Stone, M. Terrones, B. I. Yakobson, N. Alem, *Nature Communications* **2014**, *5*, 4867.
- <sup>66</sup> C. Zhu, M. Yu, J. Zhou, Y. He, Q. Zeng, Y. Deng, S. Guo, M. Xu, J. Shi, W. Zhou, L. Sun, L. Wang, Z. Hu, Z. Zhang, W. Guo, Z. Liu, *Nature Communications* **2020**, *11*, 772.
- <sup>67</sup> J.-H. Fu, J. Min, C.-K. Chang, C.-C. Tseng, Q. Wang, H. Sugisaki, C. Li, Y.-M. Chang, I. Alnami, W.-R. Syong, C. Lin, F. Fang, L. Zhao, T.-H. Lo, C.-S. Lai, W.-S. Chiu, Z.-S. Jian, W.-H. Chang, Y.-J. Lu, K. Shih, L.-J. Li, Y. Wan, Y. Shi, V. Tung, *Nature Nanotechnology* **2023**, *18*, 1289.
- <sup>68</sup> T. Li, W. Guo, L. Ma, W. Li, Z. Yu, Z. Han, S. Gao, L. Liu, D. Fan, Z. Wang, Y. Yang, W. Lin, Z. Luo, X. Chen, N. Dai, X. Tu, D. Pan, Y. Yao, P. Wang, Y. Nie, J. Wang, Y. Shi, X. Wang, *Nature Nanotechnology* **2021**, *16*, 1201.

---

<sup>69</sup> D. Dumcenco, D. Ovchinnikov, K. Marinov, P. Lazić, M. Gibertini, N. Marzari, O. L. Sanchez, Y.-C. Kung, D. Krasnozhan, M.-W. Chen, S. Bertolazzi, P. Gillet, A. F. I. Morral, A. Radenovic, A. Kis, *ACS Nano* **2015**, 9, 4611.

# Supporting Information

## **Growth of Highly Conductive PtSe<sub>2</sub> Films Controlled by Raman Metrics for High-Frequency Photodetectors and Optoelectronic Mixers at 1.55 μm**

*Eva Desgué\*, Ivan Verschueren, Marin Tharrault, Djordje Dosenovic, Ludovic Largeau, Eva Grimaldi, Delphine Pommier, Doriane Jussey, Bérangère Moreau, Dominique Carisetti, Laurent Gangloff, Patrick Plouhinec, Naomie Messudom, Zineb Bouyid, Didier Pribat, Julien Chaste, Abdelkarim Ouerghi, Bernard Plaçais, Emmanuel Baudin, Hanako Okuno, Pierre Legagneux\**

1. Determination of PtSe<sub>2</sub> film thickness by EDX
2. Optimization of PtSe<sub>2</sub> synthesis
3. State-of-the-art electrical conductivity of PtSe<sub>2</sub>
4. Air stability of PtSe<sub>2</sub>
5. Structural analysis of the as-grown and annealed samples
  - a. GIXRD  $\varphi$  scan
  - b. Domain size estimation by GIXRD
  - c. Grain boundary structures in the annealed sample
  - d. HR-STEM dark field imaging
  - e. Moiré intensity mapping for assessing the stacking quality
  - f. 4D-STEM dark field imaging
  - g. Determination of characteristic standard deviation of tilt( $\vec{c}$ )
6. Device fabrication and measurements

# 1. Determination of PtSe<sub>2</sub> film thickness by EDX

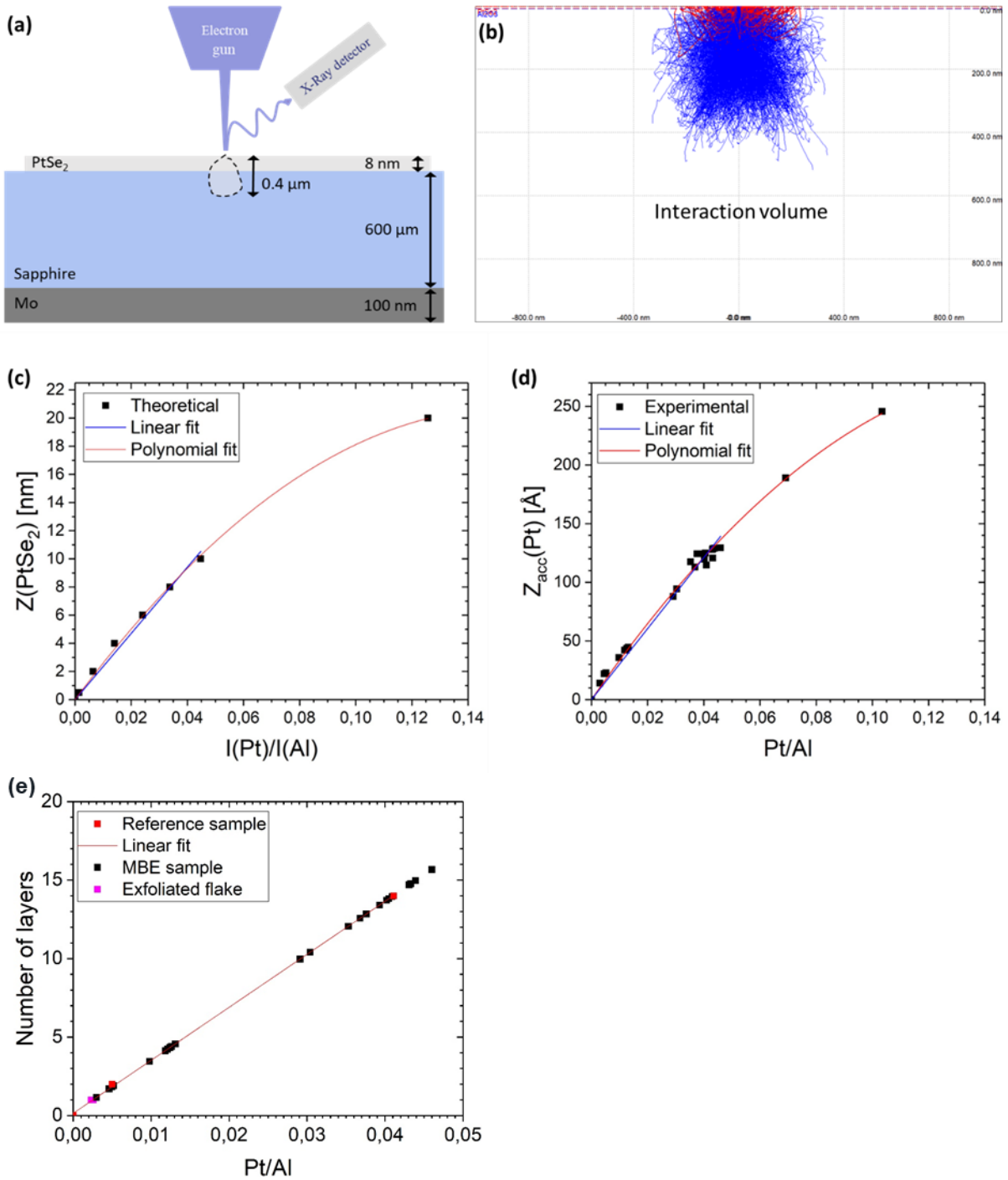


Figure S1. (a) Schematic of the MBE-grown PtSe<sub>2</sub>/sapphire samples with the electron-matter interaction volume during the EDX characterization. (b) Simulation of the interaction volume resulting from the interaction of 2000 electrons at 5 keV with a PtSe<sub>2</sub>(8 nm)/sapphire(600 μm) sample, using the Casino software. The trajectories of backscattered electrons (red) and

absorbed electrons (blue) are shown. (c) PtSe<sub>2</sub> film thickness  $Z(\text{PtSe}_2)$  as a function of the simulated intensity ratio between the Pt (M) X-ray and the Al (K) X-ray:  $I(\text{Pt})/I(\text{Al})$ . All the data are fitted with a second degree polynomial function (red curve), whereas the data for  $Z(\text{PtSe}_2)$  ranging between 0 and 9 nm are fitted with a linear function (blue curve). (d) Experimental values of the Pt thickness accumulated on the QCM during the PtSe<sub>2</sub> growth step ( $Z_{\text{acc}}(\text{Pt})$ ) as a function of the Pt/Al EDX atomic ratios of the corresponding PtSe<sub>2</sub>/sapphire samples. All the data are fitted with a second degree polynomial function (red curve), whereas the data for Pt/Al ranging between 0 and 0.05 are fitted with a linear function (blue curve). (e) Number of layers of MBE-grown PtSe<sub>2</sub>/sapphire samples as a function of their Pt/Al EDX atomic ratios. The number of layers of two reference samples (red squares) were extracted by optical absorption measurements (see method in Tharrault et al.<sup>[1]</sup>) and the results are fitted with a linear function (red line). The number of layers of our MBE samples (black squares) was calculated from the equation of the red line and their Pt/Al ratios. The number of layers of the exfoliated flake (purple squares) was determined by Raman spectroscopy.<sup>[2]</sup>

To determine the film thickness ( $Z(\text{PtSe}_2)$ ) of our PtSe<sub>2</sub> films grown on sapphire (Al<sub>2</sub>O<sub>3</sub>) substrates, we have used the atomic ratio of Pt/Al measured by EDX: Pt comes from the PtSe<sub>2</sub> film and Al comes from the substrate. This ratio is related to the film thickness as demonstrated by the simulations in Figure S1. We have simulated the corresponding electron-matter interaction with  $Z(\text{PtSe}_2)$  ranging from 0.5 to 20 nm, using the software Casino. First, at  $Z(\text{PtSe}_2) = 8$  nm (which is our main film thickness), the electron-matter interaction depth is  $\sim 400$  nm, meaning that the electron-PtSe<sub>2</sub> interaction depth is only 1/50 of the total interaction depth, as shown in Figure S1(a-b). EDX characterization uses the intensity of the non-absorbed Pt (M) X-rays and Al (K) X-rays ( $I(\text{Pt})$  and  $I(\text{Al})$ , respectively) to calculate the atomic percentages of Pt and Al present in the interaction area. This means that  $I(\text{Pt})/I(\text{Al})$  is directly related to Pt/Al. Therefore, we have secondly simulated  $I(\text{Pt})$  and  $I(\text{Al})$  for  $Z(\text{PtSe}_2)$  ranging between 0.5 and 20 nm to calculate the corresponding  $I(\text{Pt})/I(\text{Al})$  theoretical ratios, as shown in Figure S1c (black dots). These data are well fitted by a second degree polynomial function (red curve). Moreover, for  $Z(\text{PtSe}_2)$  ranging between 0 and 9 nm, which is the film thickness investigated in the present study,  $I(\text{Pt})/I(\text{Al})$  is well fitted by a line (blue curve). Therefore, the Monte Carlo simulations demonstrate that the Pt/Al atomic ratio measured by EDX is linearly linked to  $Z(\text{PtSe}_2)$  when  $Z(\text{PtSe}_2)$  is  $\leq 9$  nm.

Experimentally, we have plotted the Pt thickness accumulated on the quartz crystal microbalance (QCM) during the PtSe<sub>2</sub> growth step ( $Z_{\text{acc}}(\text{Pt})$ ) of different MBE samples, which is directly related to  $Z(\text{PtSe}_2)$ , as a function of their EDX atomic ratio of Pt/Al (Figure S1d). The data are well fitted by a second degree polynomial function (red curve), confirming that the Pt/Al ratio is a good metric to assess  $Z(\text{PtSe}_2)$ . It also shows that Pt/Al is linearly linked to  $Z_{\text{acc}}(\text{Pt})$ , and thus  $Z(\text{PtSe}_2)$ , for Pt/Al ranging from 0 to  $\sim 0.05$  (blue curve), which is in good agreement with the simulations (Figure S1c).

Note that during the EDX characterization, the scanned areas of the PtSe<sub>2</sub> samples are  $20 \times 20 \mu\text{m}^2$ , meaning that the measured atomic percentage of Pt takes into account the variations in film thickness over this area. As shown in Figure 9 of the main text, the film thickness of PtSe<sub>2</sub> samples can be inhomogeneous over small lateral distances (50 nm). Therefore, the measured Pt/Al EDX ratio is averaged over  $20 \times 20 \mu\text{m}^2$ . To calculate the number of layers ( $Z(\text{PtSe}_2)/0.51\text{nm}$ ) of our MBE-grown samples with their Pt/Al ratios, we have used references. The number of layers of two PtSe<sub>2</sub> samples was extracted by optical absorption measurements (see method in Tharrault et al.<sup>[Erreur ! Signet non défini.]</sup>). The beam spot is  $\sim 1 \mu\text{m}^2$ , meaning that the number of layers extracted by this method also takes into account the variation in film thickness over this area. The number of layers of the two reference samples was determined to be 2 and 14 MLs. These values are plotted in Figure S1e as a function of the corresponding Pt/Al ratios (red squares) and are fitted with a linear function (red line). The extracted equation of the line is used to calculate the number of layers of our MBE PtSe<sub>2</sub> samples using their Pt/Al ratios, for Pt/Al values  $< 0.05$  (black squares). To show the relevance of this calibration curve, we have also plotted the Pt/Al ratios of a monolayer monocrystalline flake obtained by ME (purple squares), which fit very well with the calibration curve.

## 2. Optimization of PtSe<sub>2</sub> synthesis

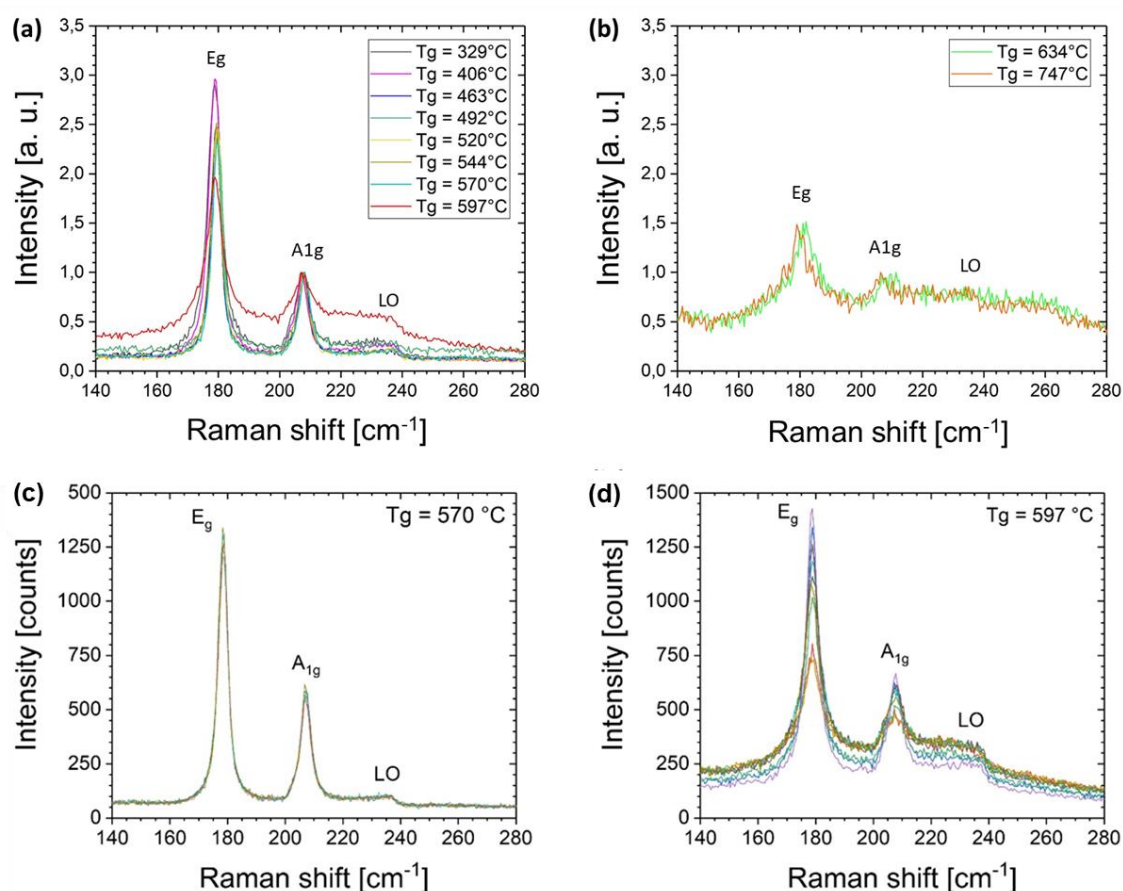


Figure S2. (a - b) Raman spectra ( $\lambda = 532$  nm) of MBE-grown PtSe<sub>2</sub> films synthesized at different growth temperatures (T<sub>g</sub>) under  $0.2 \text{ \AA}\cdot\text{s}^{-1}$  of Se. The intensity of the spectra is normalized to the A<sub>1g</sub> peak. The Raman shift of the different spectra is not calibrated, the peak position is thus arbitrary. (c - d) Raman spectra acquired at 9 different sample positions of the PtSe<sub>2</sub> films synthesized at T<sub>g</sub> = 570 °C and T<sub>g</sub> = 597 °C, respectively.

Figure S2(a-b) show that the 3 characteristic Raman peaks of PtSe<sub>2</sub> are observed for all the T<sub>g</sub> values. However, from T<sub>g</sub> = 597 °C (red curve in Figure S2a), the background level and the FWHM of the E<sub>g</sub> and A<sub>1g</sub> peaks strongly increase, and from T<sub>g</sub> = 634 °C (green curve in Figure S2b), the Raman signal becomes very weak and the Raman peaks are no longer well defined. This indicates that the crystalline quality deteriorates from T<sub>g</sub> = 597 °C. Moreover, Figure S2d shows that the Raman spectra acquired at 9 different positions of the sample synthesized at T<sub>g</sub> = 597 °C are very inhomogeneous (for comparison, Figure S2c displays the 9 Raman spectra



of the sample synthesized at  $T_g = 570$  °C). This inhomogeneity is highlighted by the strong dispersion of both the  $E_g$  and  $A_{1g}$  FWHM values (large vertical bars in Figure 2b of the main text) and indicates a strong film inhomogeneity.

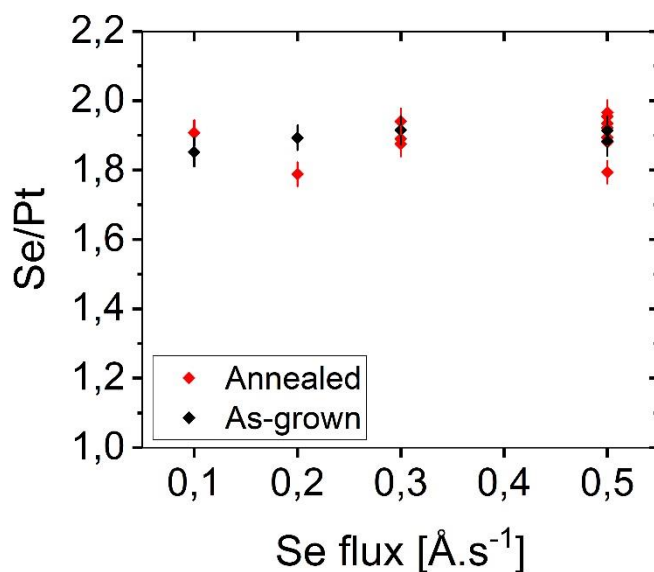


Figure S3. Se/Pt atomic ratios of MBE-grown PtSe<sub>2</sub> films extracted from EDX measurements. Samples are synthesized at 520 °C without (black dots) or with (red dots) a post-growth annealing at 690 °C for 30 min, under different Se fluxes. The vertical bars correspond to the error on the Se/Pt ratio values.

Figure S3 shows that there is no obvious relationship between the Se/Pt EDX atomic ratio of samples and the Se flux implemented during the synthesis. There is also no significant change in the ratio between as-grown and annealed samples, demonstrating that no desorption of Se occurs during the post-growth annealing under Se flux.

### 3. State-of-the-art electrical conductivity of PtSe<sub>2</sub>

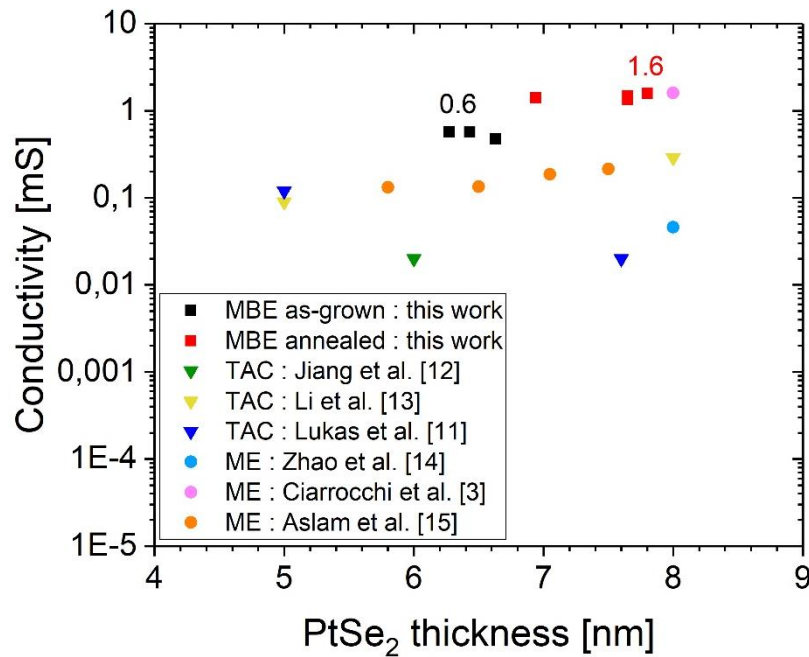


Figure S4. State-of-the-art electrical conductivities of PtSe<sub>2</sub> films as a function of their thickness. The samples were synthesized using different methods: mechanical exfoliation (ME) of a bulk crystal, thermally assisted conversion (TAC) and MBE in this study. In this graph, the MBE as-grown samples are synthesized under different Se fluxes, while the MBE annealed samples plotted are synthesized only under 0.5 Å.s<sup>-1</sup>. Note that the highest conductivity value of 1.6 mS found in the literature (pink disk) has been measured at 10 K.<sup>[3]</sup>

Figure S4 shows that both our as-grown (black squares) and annealed (red squares) PtSe<sub>2</sub> films synthesized by MBE exhibit higher conductivities compared to TAC samples and to most of exfoliated samples. Moreover, our maximal value of 1.6 mS is as high as the best value reported, which correspond to an exfoliated PtSe<sub>2</sub> film of similar thickness, i.e. 8 nm<sup>[3]</sup> (pink disk).

## 4. Air stability of PtSe<sub>2</sub>

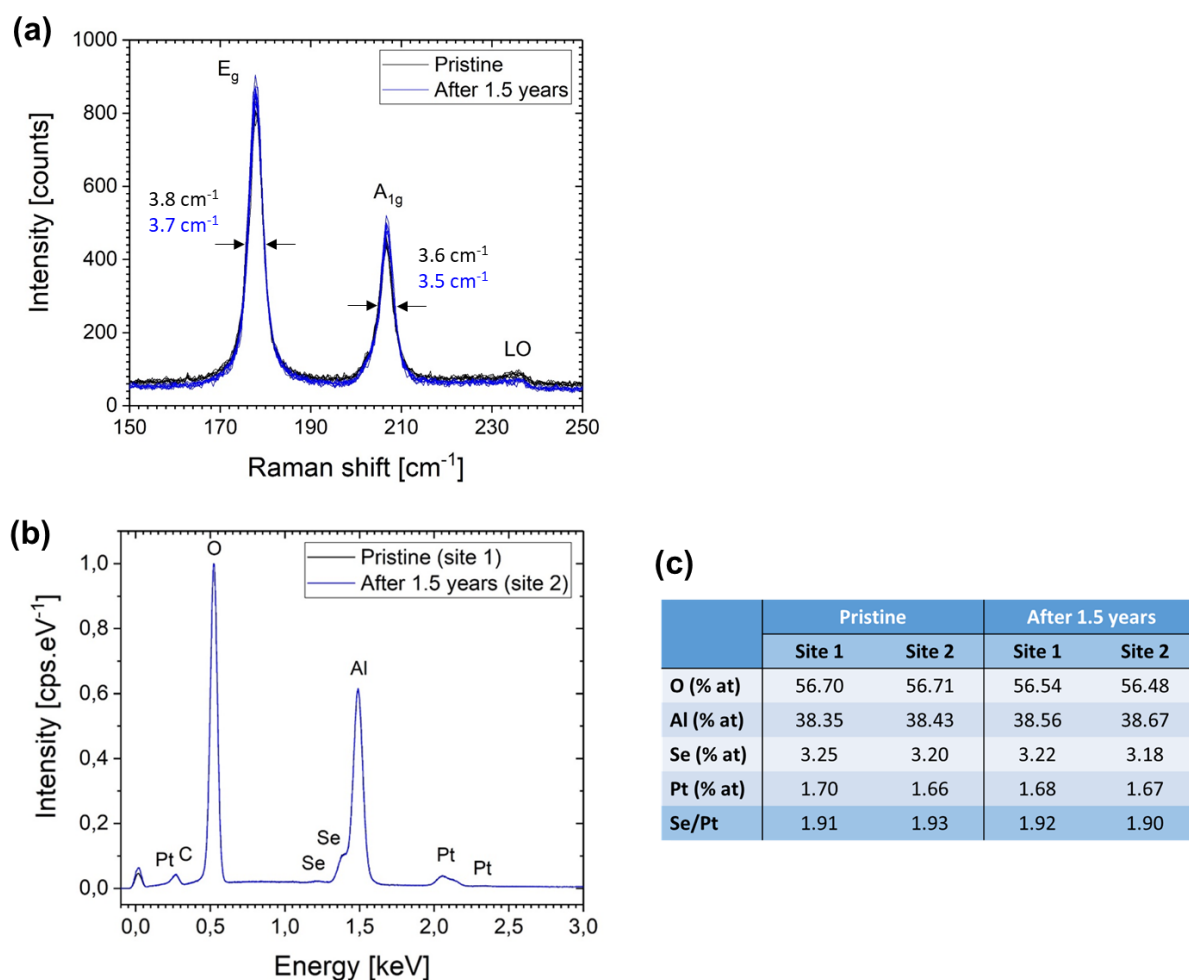


Figure S5. (a) Raman spectra ( $\lambda = 532$  nm) recorded on a MBE-grown annealed PtSe<sub>2</sub> sample a few days after the synthesis (black curves) and after 1.5 years in air (blue curves). The corresponding median FWHM values of the E<sub>g</sub> and A<sub>1g</sub> peaks are displayed. (b) EDX spectra of the corresponding PtSe<sub>2</sub>/Al<sub>2</sub>O<sub>3</sub> sample measured a few days after synthesis (black curve) and after 1.5 years in air (blue curve). (c) Table showing the atomic percentages extracted from the EDX spectra and the calculated atomic ratios of Se/Pt from two different analyzed areas (site 1 and site 2) of the sample.

## 5. Structural analysis of the as-grown and annealed samples

### a. GIXRD $\varphi$ scan

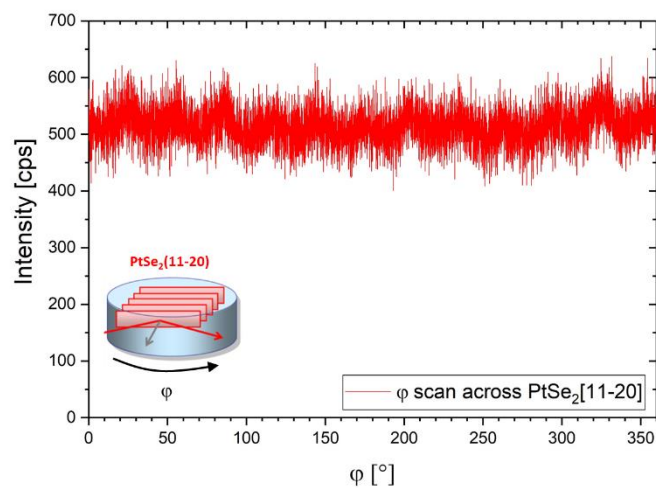


Figure S6. GIXRD azimuthal ( $\varphi$ ) scan across the  $\text{PtSe}_2[11-20]$  direction of an annealed  $\text{PtSe}_2$  film. The X-ray detector was positioned at the angle corresponding to the diffraction of the  $\text{PtSe}_2(11-20)$  planes and the sample was rotated azimuthally over  $360^\circ$ . The intensity of the  $\text{PtSe}_2(11-20)$  diffraction peak is plotted as a function of the azimuthal angle ( $\varphi$ ). The isotropic signal indicates that the  $\text{PtSe}_2$  domains have random in-plane orientations.

## b. Domain size estimation by GIXRD

The in-plane domain size of the samples was first calculated using the Scherrer formula (S1), which has resulted in size values (D) exhibiting a strong variation with the diffraction angle,<sup>[4]</sup> as shown in Table S1. The Scherrer formula neglects the contribution of non-uniform lattice distortions (microstrains), which also produce a significant broadening of the X-ray diffraction peaks.<sup>[5]</sup>

As-grown sample				Annealed sample			
hkil	$2\theta_\chi$ [°]	$\Delta(2\theta_\chi)_{\text{meas}}$ [°]	D [Å]	hkil	$2\theta_\chi$ [°]	$\Delta(2\theta_\chi)_{\text{meas}}$ [°]	D [Å]
10-10	27.82031	0.5252	255.7617409	10-10	27.70473	0.481	329.4913909
11-20	49.23445	0.6579	176.1212809	11-20	48.99778	0.548	247.1201257
20-20	57.53772	0.7215	158.6028808	20-20	57.17303	0.5964	215.9398321
30-30	92.42317	1.1502	111.4334124	30-30	91.81508	0.8539	158.702245
22-40	112.822	1.5485	100.3962598	22-40	112.025	1.0445	154.2406319

Table S1. Analysis of the in-plane domain size of the as-grown and annealed PtSe<sub>2</sub> films. The in-plane domain size (D) of the samples is calculated using the Scherrer formula:

$$D = \frac{K\lambda}{\Delta(2\theta_\chi)\cos(\theta_\chi)} \quad (\text{S1})$$

where K is the Scherrer constant (0.94 for isotropic crystallites),  $\lambda$  is the X-ray wavelength (1.54056 Å),  $2\theta_\chi$  is the diffraction angle and  $\Delta(2\theta_\chi)$  is the peak FWHM deconvoluted from the instrument width, such as:

$$\Delta(2\theta_\chi) = \sqrt{\Delta(2\theta_\chi)_{\text{meas}}^2 - \Delta(2\theta_\chi)_{\text{instru}}^2} \quad (\text{S2}) \quad \text{with } \Delta(2\theta_\chi)_{\text{instru}} = 0.405^\circ$$

Equation S1 gives domain size values (D) exhibiting a strong variation with the diffraction angle ( $2\theta_\chi$ ) for both samples. For example, the FWHM ( $\Delta(2\theta_\chi)_{\text{meas}}$ ) of the PtSe<sub>2</sub>(11-20) and PtSe<sub>2</sub>(22-40) diffraction peaks of the annealed sample give calculated D values of 25 and 15 nm, respectively, even though these planes belong to the same family. Such a meaningless result reveals that not only the limited size of the crystallites is at the origin of the diffraction peak broadening. Therefore, the classical Scherrer formula cannot be applied in this case.

We then implemented the Williamson-Hall method<sup>[6]</sup> to evaluate the contribution of the in-plane domain size ( $D_{\text{WH}}$ ) and the lattice microstrain ( $\epsilon$ ) to the peak broadening (see e.g. for WSe<sub>2</sub><sup>[7]</sup>). According to this model:

$$\Delta(2\theta_{\chi})_{\text{size}} = \frac{K\lambda}{D_{\text{WH}}\cos(\theta_{\chi})} \quad (\text{S3})$$

$$\Delta(2\theta_{\chi})_{\text{strain}} = 4\epsilon\tan(\theta_{\chi}) \quad (\text{S4})$$

Thus, injecting equation S3 and S4 into equation S1 gives:

$$\Delta(2\theta_{\chi})\cos(\theta_{\chi}) = \frac{K\lambda}{D_{\text{WH}}} + 4\epsilon\sin(\theta_{\chi}) \quad (\text{S5})$$

In Figure 5b of the main text,  $\Delta(2\theta_{\chi})\cos(\theta_{\chi})$  is plotted as a function of  $\sin(\theta_{\chi})$  and fitted with a linear function. For both the as-grown and annealed samples, the experimental data are well fitted by lines, as predicted by the method. From the slope and y-intercept, we derive  $D_{\text{WH}}$  and  $\epsilon$  values shown in Table S2.

	Intercept = $K\lambda/D_{\text{WH}}$	Slope = $4\epsilon$	$D_{\text{WH}}$ [ $\text{\AA}$ ]	$\epsilon$ [%]
As-grown	$0.002 \pm 1.477\text{E-}4$	$0.01501 \pm 2.54957\text{E-}4$	$724 \pm 54$	$0.38 \pm 0.0064$
Annealed	$0.0023 \pm 3.89448\text{E-}4$	$0.00895 \pm 6.75578\text{E-}4$	$630 \pm 107$	$0.22 \pm 0.017$

Table S2. Williamson-Hall plot data for the as-grown and annealed samples.

c. Grain boundary structures in the annealed sample

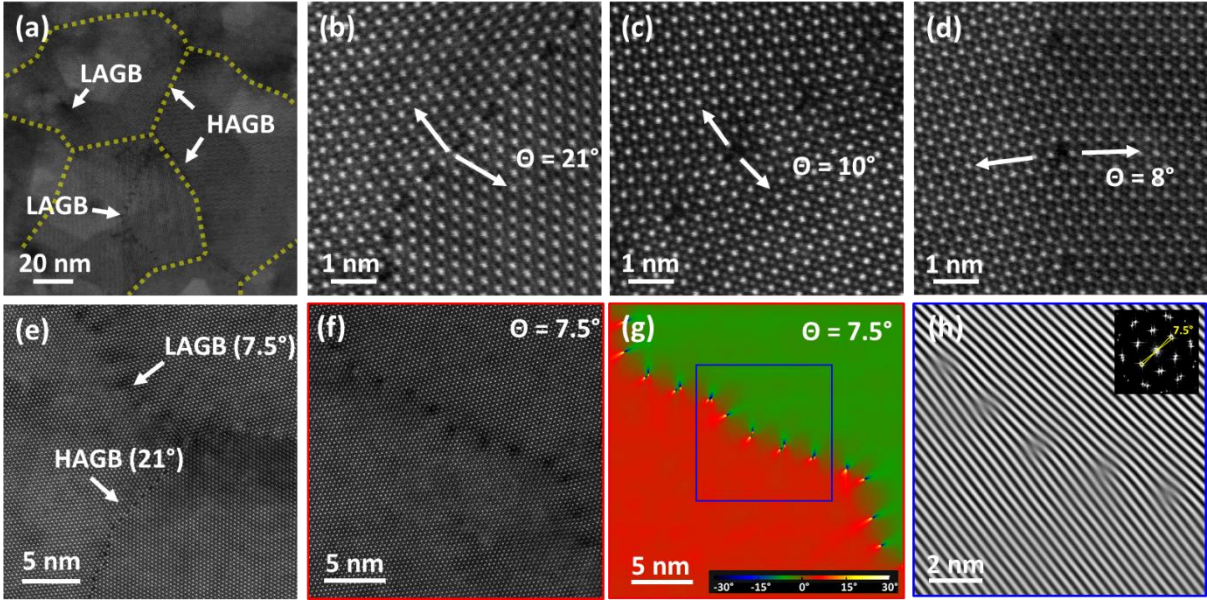
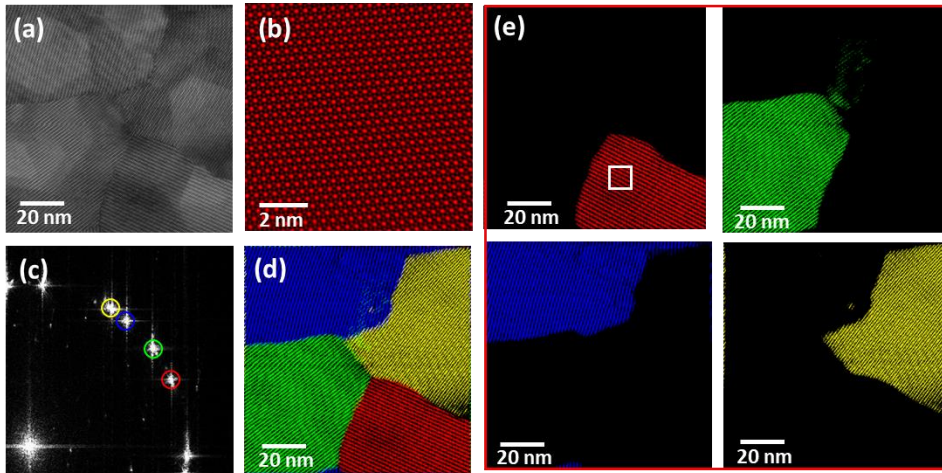


Figure S7. (a - f) HAADF-STEM images of grain boundaries between grains misoriented by an angle  $\theta$ , observed in the annealed PtSe<sub>2</sub> sample. (g) Orientation field map obtained by Geometric Phase Analysis (GPA) for the area shown in (f). The color scale corresponds to the relative in-plane angle. (h) Dislocation cores visualized by FFT filtering for the PtSe<sub>2</sub>(10-10) spot, as shown in the inset.

As shown in Figure S7a and S7e, two types of grain boundaries (GBs) are observed in the annealed sample. The first type consists of crystalline domains with in-plane sizes ranging from 50 to 80 nm, surrounded by continuous line defects, as indicated by the yellow dashed lines. These line defects are generally GBs formed between two crystalline grains misoriented by relatively high angles ( $\theta > \sim 10^\circ$ ), the so-called HA (high angle) GBs. HAGBs are typically composed of a combination of 5 - 7 rings, as studied in the literature for monolayer PtSe<sub>2</sub>.<sup>[8]</sup> In these crystalline domains, small-angle misorientations are additionally investigated. The neighboring domains misoriented by relatively small angles ( $\theta < \sim 10^\circ$ ) are connected by LA (low angle) GBs consisting of several dislocation cores aligned in a line, as shown in Figure S7c, S7d and S7f. The standoff distance between dislocation cores increases as the misorientation angle decreases. The crystal structures are not completely disrupted, as the crystal planes remain connected across the two domains, even in the presence of dislocations, (as shown by GPA analyses in Figure S7(g-h)).

d. HR-STEM dark field imaging

**Post-growth annealed sample**



**As-grown sample**

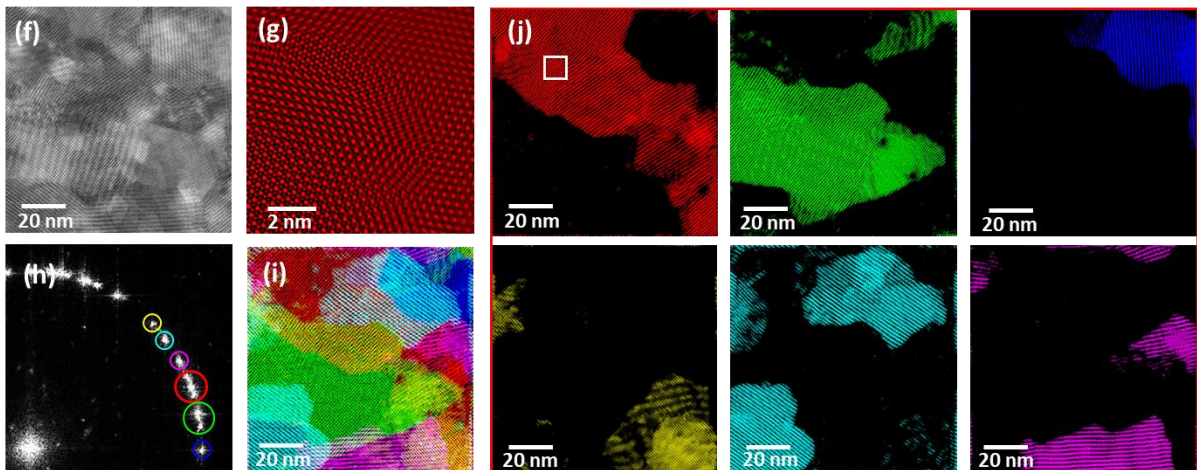


Figure S8. (a) and (f) are HAADF-STEM images of the annealed and as-grown PtSe<sub>2</sub> samples, respectively. (d) and (i) are the corresponding superimposed DF images obtained from selected FFT spots shown in (c) and (h), respectively. (b) and (g) show typical projected structures in an individual domain, extracted from the white squares in the domain indicated in red in (e) and (j), respectively. (e) and (j) are individual DF images for a selected area in the FFT indicated by the color codes in (c) and (h), respectively.

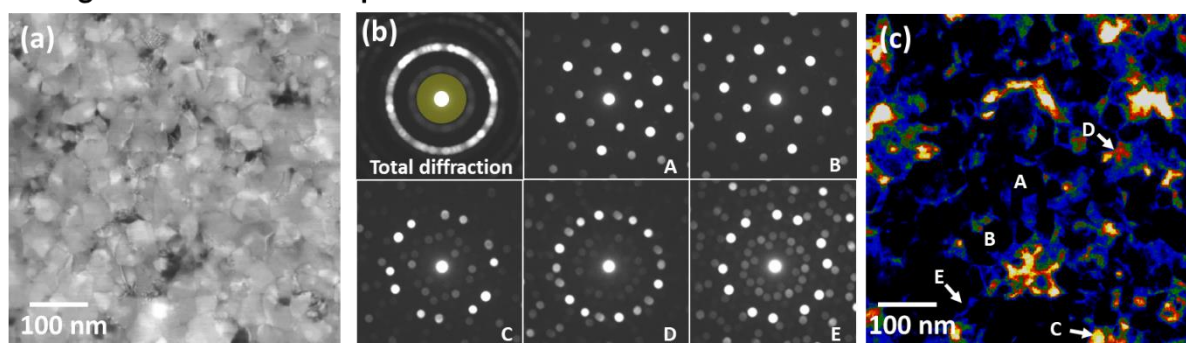
Figure S8 shows atomic resolution images of the annealed and as-grown samples and the corresponding FFT-based DF images. The annealed sample consists of a lateral conjunction of domains clearly identified by a single spot in the FFT (Figure S8(c-e)), with sharp GBs. In contrast, in the as-grown sample, several domains are identified where 2 to 4 domains with



different in-plane orientation ranges are locally superimposed within the film thickness, as shown in Figure S8i. These domains are often not perfectly single crystalline, but contain slight local in-plane misorientation or defects in individual layers. For example, two domains illuminated in red and green in Figure S8j exhibit several spots spread within a small angular range ( $7.5^\circ$ ), as indicated by red and green circles in the FFT (Figure S8h). Figure S8g also shows a sliding effect in the projected atomic images which suggests defective feature of as-grown domains.

e. Moiré intensity mapping for assessing the stacking quality

**Post-growth annealed sample**



**As-grown sample**

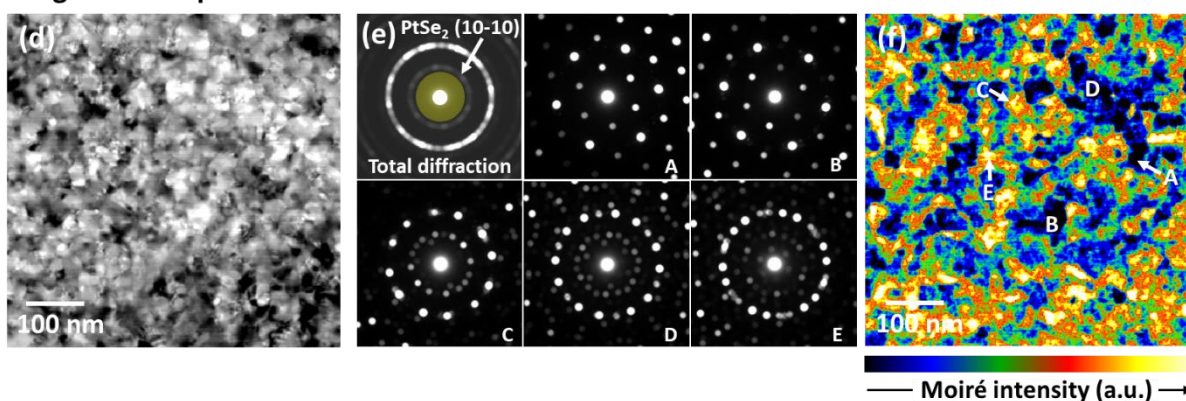


Figure S9. (a) and (d) ADF images reconstructed from 4D-datasets of the annealed and as-grown films, respectively. (b) and (e) total diffraction pattern for  $400 \times 400$  pixels and individual local diffraction patterns for selected positions (A to E) indicated in (c) and (f), respectively. (c) and (f) moiré intensity maps of the annealed and as-grown films, respectively. The total intensity of the moiré signals is accumulated in the area indicated by the yellow disks in (b) and (e).

The 4D datasets were used to extract local stacking information for comparing the stacking quality of domains in the annealed and as-grown films. The total intensity of the moiré signals, which appear due to multiple diffractions, is extracted from the region between the transmitted beam and the PtSe<sub>2</sub>(10-10) spots, marked by yellow disks in Figure S10b and S10e. This region corresponds to  $0.69 < 1/d < 2.25 \text{ nm}^{-1}$ . The moiré intensity maps (Figure S10c and S10f) are reconstructed from these total intensities. Since often 2 to 4 misoriented domains are superimposed, the position of the moiré spots is not straight forward to the twist angles. Some moiré spots, appearing between 0 and 0.69 and 2.25 and 2.70  $\text{nm}^{-1}$ , cannot be included due to the width of the diffraction spot (= 1 mrad), so that this imaging mode does not provide precise quantitative information. It should also be noted that the variation in local thickness affects the overall intensity of the moiré signal. Nevertheless, this image reconstruction reflects well the local stacking state, as shown by the diffraction spots in Figure S10b and S10e, for the corresponding positions in the reconstructed images. Therefore, the inverse of the moiré intensity maps, reconstructed in Figure 8c and 8g of the main text, can serve as an efficient tool to monitor the stacking quality of the PtSe<sub>2</sub> films, in particular, for identifying vertically single crystalline regions characterized by single diffraction spots.

f. 4D-STEM dark field imaging

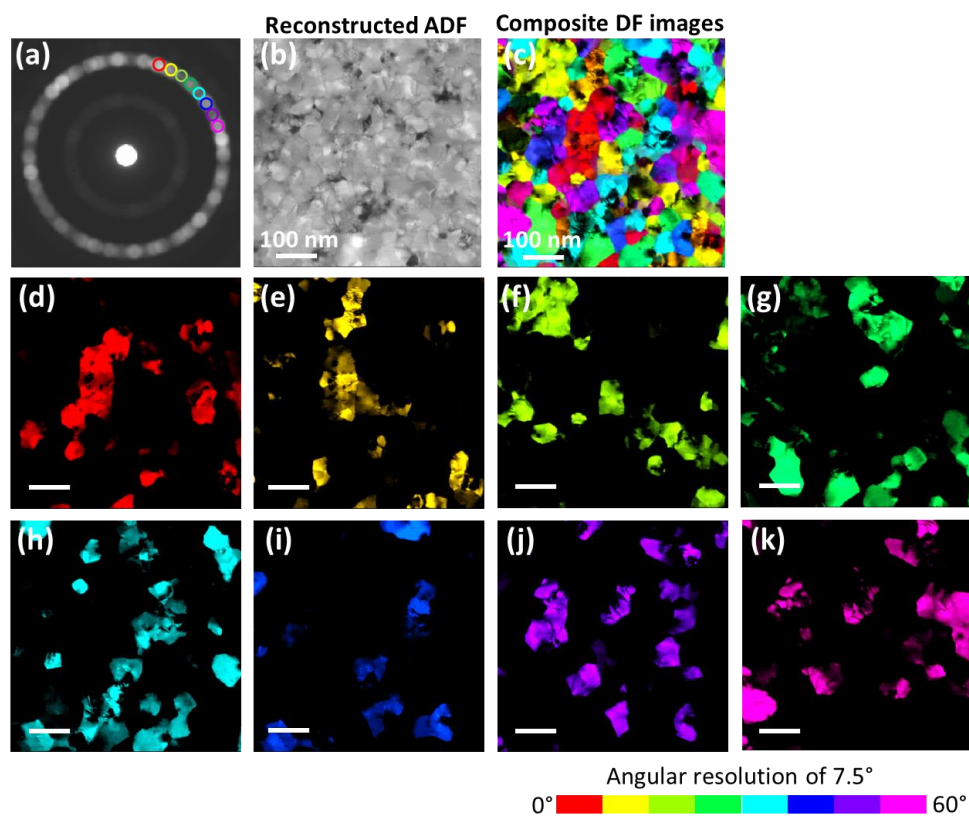


Figure S10. 4D-STEM DF analysis of the post-growth annealed sample shown in Figure 7 of the main text. (a) Total diffraction pattern and (b) virtual ADF image. (c) Superimposed and (d - k) separated DF images illuminated for the corresponding angular range ( $7.5^\circ$ ) in the diffraction pattern. The color code is shown in the color bar.

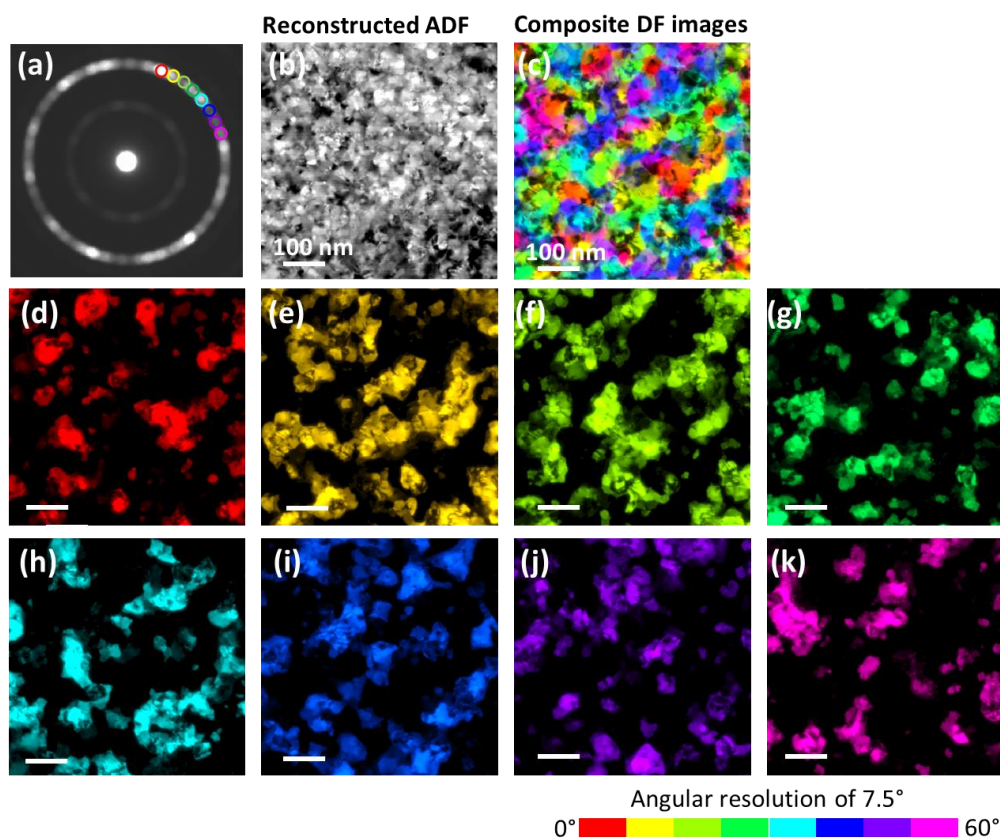


Figure S11. 4D-STEM DF imaging of the as-grown sample shown in Figure 8 of the main text. (a) Total diffraction pattern and (b) virtual ADF image. (c) Superimposed and (d - k) separated DF images illuminated for the corresponding angular range ( $7.5^\circ$ ) in the diffraction pattern. The color code is shown in the color bar.

The 4D-datasets used for the orientation mapping in Figure 8d and 8h of the main text were also analyzed using filtering. Figures S10 and S11 show DF images of the annealed and as-grown samples, respectively, obtained by the signal separation for a selected angular range ( $7.5^\circ$ ). Figure S10 shows that the annealed film is relatively well separated into angular selected domains in the in-plane direction. On the contrary, Figure S11 shows that, in the as-grown sample, several domains illuminated with different angular ranges are often found at the same position. This indicates that the domains with different in-plane orientations are distributed in both lateral and vertical directions. The domain size determined with an angular range of  $7.5^\circ$  was between 50 and 80 nm. It should be noted that within  $7.5^\circ$  the high-resolution analysis shows a widely spread angular variation (Figure S8h). This confirms that the domains are not really single crystalline, but should contain an important amount of defects, such as dislocations and LAGBs, which could lead to local in-plane strain, as shown by the GIXRD analysis. This

large area analysis confirms: i) the superimposition of twisted domains in the as-grown sample and ii) the improvement in the vertical alignment of domains induced by the annealing process.

g. Determination of characteristic standard deviation of tilt( $\vec{c}$ )

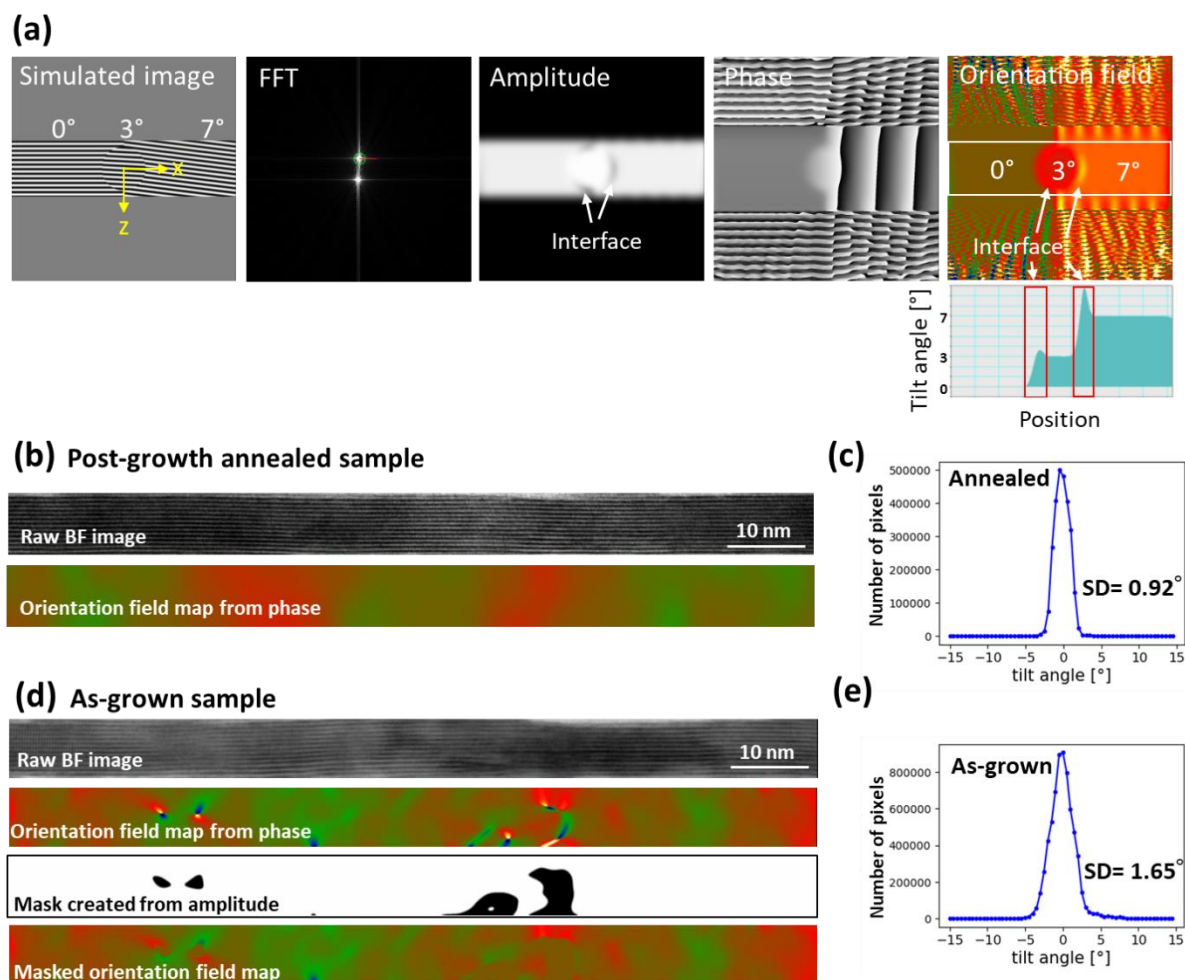


Figure S12. (a) GPA analysis process using a simulated interface model. (b) Bright field (BF) image and corresponding orientation field map of the annealed sample and (c) histogram of tilt( $\vec{c}$ ) values extracted from the orientation field map with the characteristic standard deviation (SD) value. (d) BF image, corresponding orientation field map of the as-grown sample, mask created to remove interface effects and the resulting masked orientation field map. (e) Histogram of tilt( $\vec{c}$ ) values extracted from the masked orientation field map with the characteristic standard deviation (SD) value.

To quantitatively assess the flatness of the films, the standard deviation (SD) of the local out-of-plane tilt angle with respect to the sapphire c-plane,  $\text{tilt}(\vec{c})$ , was measured from cross-sectional STEM images using GPA.<sup>[9,10]</sup> Bright field (BF) STEM images are used for better image contrast. The orientation field map, consisting of quantitative values of  $\text{tilt}(\vec{c})$  at each pixel, is generated using the GPA plug-in (digital micrograph) and these values are then collected to create histograms and further calculate the SD  $\text{tilt}(\vec{c})$ . Although the local  $\text{tilt}(\vec{c})$  values obtained from the GPA orientation field map are reliable, the artifact that appears at the interface between different angles provides artificially intense lines. Figure S12a shows the process flow for obtaining the orientation field maps, where the simulated structural model, consisting of 3 domains with different angles, is used to examine the interface effect. As shown in the line profile extracted from the orientation field map, the artificially intense lines appear at the interface (indicated by the red squares). To remove these artifacts from the statistical local  $\text{tilt}(\vec{c})$  analysis, we create a mask based on the amplitude image using the threshold optimized with simulated images. Figure S12b and S12d show the orientation field maps, as well as the original BF STEM images, of the annealed and the as-grown films respectively. The annealed film generally shows unidirectional (in-plane direction) corrugation, while the as-grown film shows a more frequent variation of the  $\text{tilt}(\vec{c})$  in both in-plane and out-of-plane directions. This often induces the artificial intense lines due to the interface effect. The mask is then used for the as-grown sample to remove these artifacts, in order to collect only the  $\text{tilt}(\vec{c})$  values that originates from the local layer orientation. Figure S12c and S12e display the histograms of  $\text{tilt}(\vec{c})$  values collected at each pixel in several images, covering a total analyzed region in length of 600 nm to ensure reliable statistical analysis, where the collection area length (600 nm) was chosen for a reliable comparison with SD  $\text{tilt}(\vec{c})$  values for TAC samples given in the literature<sup>[11]</sup> (presented in section 2.4 of the main text). The characteristic SD  $\text{tilt}(\vec{c})$  values over 600 nm obtained from these histograms are 0.92 ° and 1.65 ° for the annealed and the as-grown films, respectively. The number of pixels in the masked areas is removed from the total population for these calculations. It should be noted that reducing the collection area length to around the in-plane domain size allows the SD  $\text{tilt}(\vec{c})$  values to better reflect local out-of-plane tilt disorders, such as the planarity of individual layers comparable to the “c” values measured by HRXRD.

## 6. Device fabrication and measurements

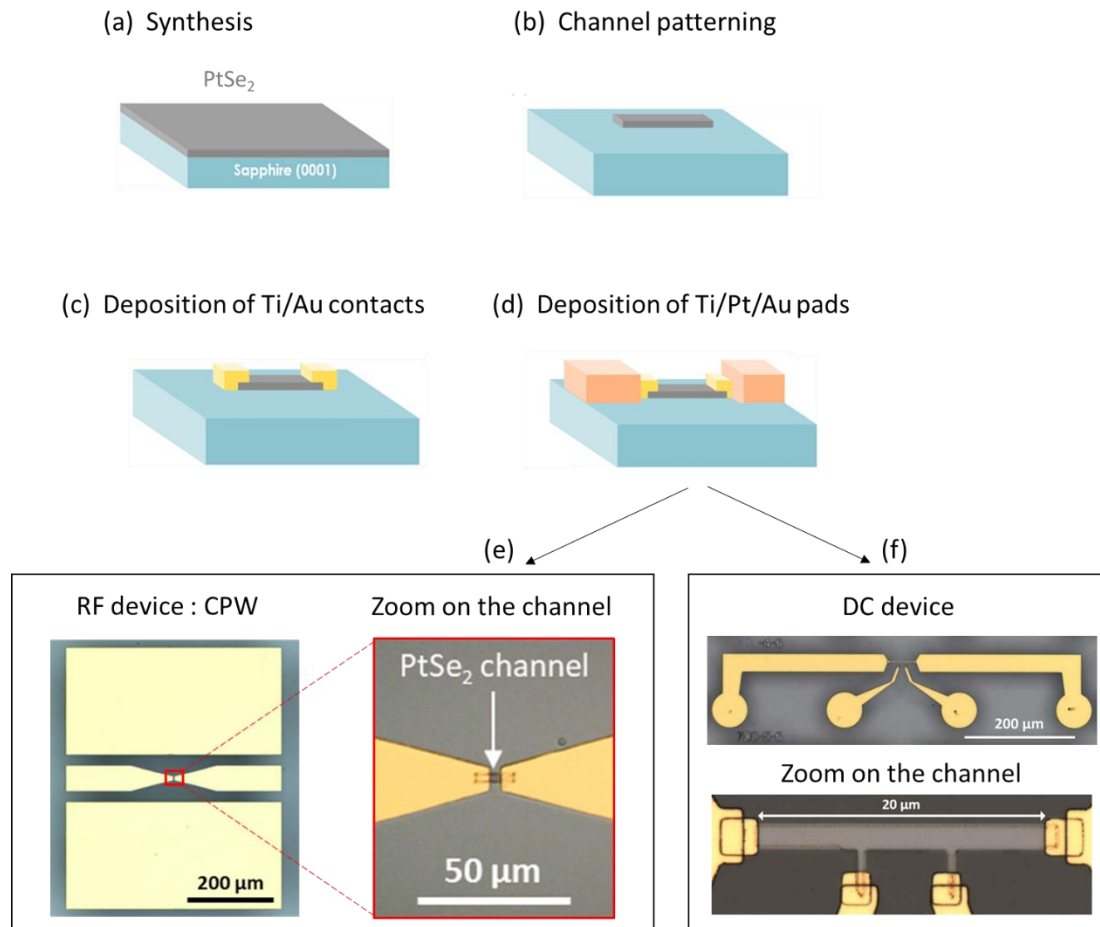


Figure S13. Fabrication steps of the PtSe<sub>2</sub>-based devices. (a) A 14 ML PtSe<sub>2</sub> film was synthesized by MBE on a 2-inch sapphire substrate, (b) PtSe<sub>2</sub> channels were patterned and etched by RIE (SF<sub>6</sub>/Ar), (c) after optical lithography steps, an electron beam evaporator was used to deposit Ti(10nm)/Au(100nm) metal contacts and then (d) Ti(20nm)/Pt(20nm)/Au(200nm) metal pads. This last step also allowed the definition of the coplanar waveguides (CPWs) for the RF devices. (e) and (f) show optical images of the RF device integrating CPW and of the DC device, respectively.

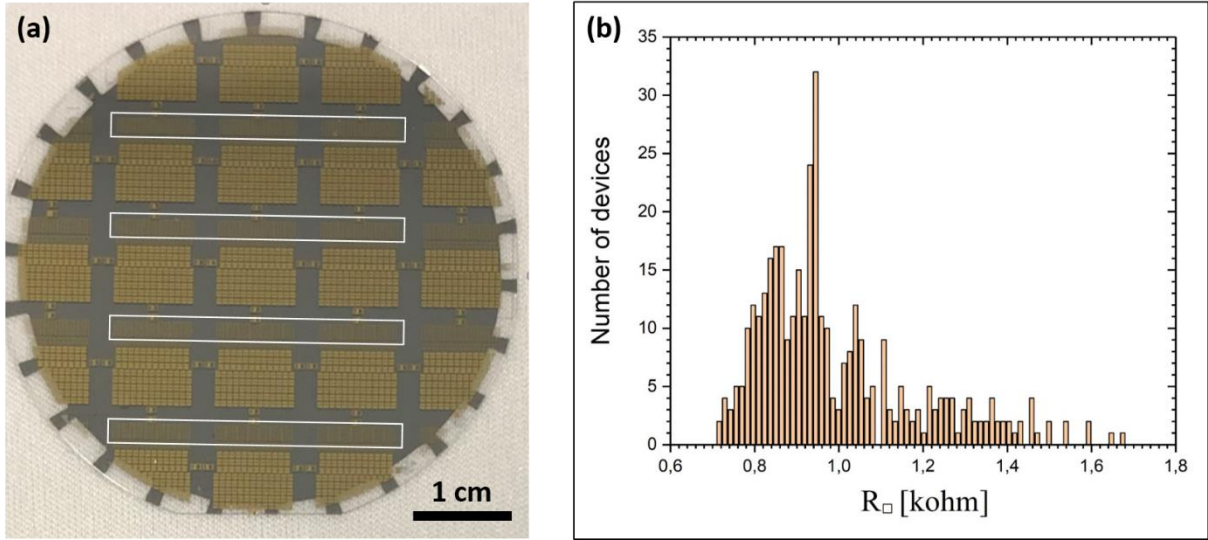


Figure S14. (a) PtSe<sub>2</sub>-based devices fabricated on a 2-inch sapphire substrate with the measured DC devices enclosed in white rectangles. (b) Histogram showing the dispersion of the  $R_{\square}$  values over the 378 devices.

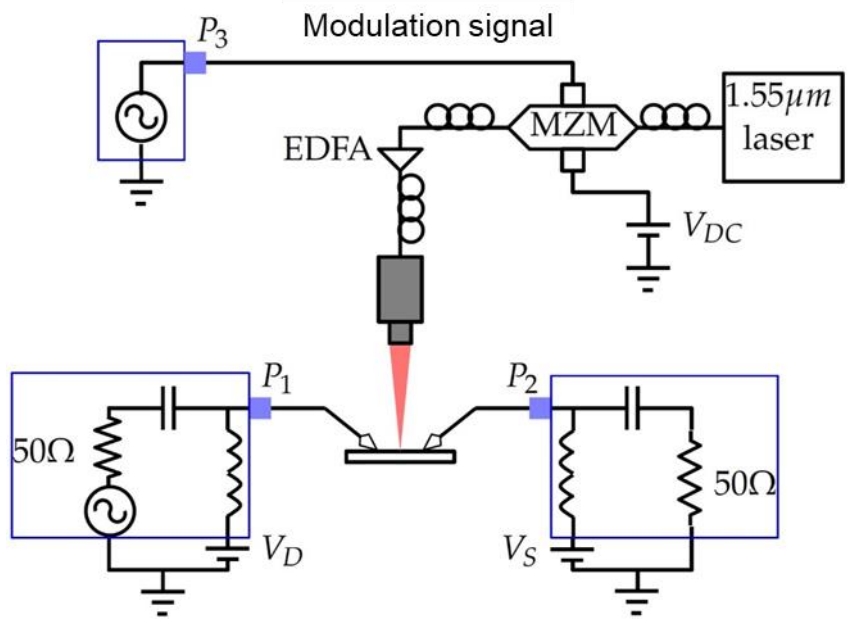


Figure S15. Detailed schematic of the experimental setup used to measure the photodetection and optoelectronic mixing. The optical signal is generated by a 1.55  $\mu\text{m}$  laser. Its intensity is modulated by a Mach Zehnder modulator (MZM) using a local oscillator (LO) signal at  $f_{\text{opt}}$  generated from port 3 (P3) of the virtual network analyzer (VNA). The MZM operation is also controlled by a DC bias ( $V_{\text{DC}}$ ). The optical signal is amplified by an erbium-doped amplifier (EDFA) and is focused onto the PtSe<sub>2</sub> channel of the device (the laser spot diameter is 2.5  $\mu\text{m}$ ).



The VNA is internally equipped with a bias T (capacitor and inductor in the schematic) to allow the application of drain-source biases ( $V_D$ ,  $V_S$ ) from external DC source measure units (SMUs). The input RF or DC signal is injected from port 1 (P1) and the mixing and photodetection output signal is received at port 2 (P2).

Photodetection: A RF signal ( $f_{\text{opt}} = 2 - 67$  GHz) generated by port 3 (P3) of the VNA is applied to the MZM to modulate the optical signal. PtSe<sub>2</sub> acts as a photoconductor thus, the PtSe<sub>2</sub> channel is biased through a probe from port 1 (P1) with  $V_D = 4$  V and  $V_S = 0$  V and another RF probe measures the signal generated by the device at the same frequency ( $f_{\text{opt}}$ ) at port 2 (P2) of the VNA.

Optoelectronic mixing:  $f_{\text{opt}}$  is fixed at 30 GHz. A RF signal ( $f_{\text{RF}} = 0.01 - 29.99$  GHz) generated by port 1 (P1) of the VNA is applied to the device using an RF probe. Another RF probe measures the signal generated by the device in the intermediate frequency band ( $f_{\text{IF}} = f_{\text{opt}} - f_{\text{RF}}$ ) at port 2 (P2) of the VNA. As the PtSe<sub>2</sub> channel is biased by the input RF signal, no DC bias is required:  $V_S = V_D = 0$  V.

For both RF measurements, a ZVA67 system from Rohde&Schwarz is used. The system has been calibrated up until the RF probes. The light is modulated using a MXAN-LN-40 MZM from iXBlue Photonics. For  $f_{\text{opt}}$  up to 33.5 GHz, the system is used in quadrature mode (transmission = 50 %), where the light modulation frequency is the RF frequency from P3 ( $f_{\text{RF3}}$ ) applied to the MZM:  $f_{\text{opt}} = f_{\text{RF3}}$ . For  $f_{\text{opt}}$  between 33.5 GHz and 67 GHz, we use the minimum mode (transmission = 0 %), where the light modulation results from the beatings between the optical components at  $f_0 - f_{\text{RF3}}$  and  $f_0 + f_{\text{RF3}}$ , (where  $f_0$  is the 1.55  $\mu\text{m}$  light frequency), thus the light is modulated at twice the applied RF frequency:  $f_{\text{opt}} = 2 \times f_{\text{RF3}}$ .

## References

---

- [1] M. Tharrault, S. Ayari, M. Arfaoui, E. Desgué, R. L. Goff, P. Morfin, J. Palomo, M. Rosticher, S. Jaziri, B. Plaçais, P. Legagneux, F. Carosella, C. Voisin, R. Ferreira, E. Baudin, *Phys. Rev. Lett.* **2025**, *134*, 066901
- [2] M. Tharrault, E. Desgué, D. Carisetti, B. Plaçais, C. Voisin, P. Legagneux, E. Baudin, *2D Mater.* **2024**, *11*, 025011.
- [3] A. Ciarrocchi, A. Avsar, D. Ovchinnikov, A. Kis, *Nat Commun* **2018**, *9*, 919.
- [4] H. Lin, R. Wang, H. Zobeiri, T. Wang, S. Xu, X. Wang, *Nanoscale* **2021**, *13*, 7723.
- [5] A. R. Stokes, A. J. C. Wilson, *Proc. Phys. Soc.* **1944**, *56*, 174.
- [6] G. K. Williamson, W. H. Hall, *Acta Metallurgica* **1953**, *1*, 22.
- [7] Md. Akhtaruzzaman, Md. Shahiduzzaman, N. Amin, G. Muhammad, M. A. Islam, K. S. B. Rafiq, K. Sopian, *Nanomaterials* **2021**, *11*, 1635.
- [8] J. Chen, Y. Wang, W. Xu, Y. Wen, G. H. Ryu, J. C. Grossman, J. H. Warner, *ACS Nano* **2021**, *15*, 16748.
- [9] M. J. Hÿtch, E. Snoeck, R. Kilaas, *Ultramicroscopy* **1998**, *74*, 131.
- [10] J. L. Rouvière, E. Sarigiannidou, *Ultramicroscopy* **2005**, *106*, 1.
- [11] S. Lukas, O. Hartwig, M. Prechtel, G. Capraro, J. Bolten, A. Meledin, J. Mayer, D. Neumaier, S. Kataria, G. S. Duesberg, M. C. Lemme, *Adv Funct Materials* **2021**, *31*, 2102929.
- [12] W. Jiang, X. Wang, Y. Chen, G. Wu, K. Ba, N. Xuan, Y. Sun, P. Gong, J. Bao, H. Shen, T. Lin, X. Meng, J. Wang, Z. Sun, *InfoMat* **2019**, *1*, 260.
- [13] L. Li, K. Xiong, R. J. Marstell, A. Madjar, N. C. Strandwitz, J. C. M. Hwang, N. McEvoy, J. B. McManus, G. S. Duesberg, A. Goritz, M. Wietstruck, M. Kaynak, *IEEE Transactions On Electron Devices* **2018**, *65*, 4102.
- [14] Y. Zhao, J. Qiao, Z. Yu, P. Yu, K. Xu, S. P. Lau, W. Zhou, Z. Liu, X. Wang, W. Ji, Y. Chai, *Advanced Materials* **2017**, *29*, 1604230.
- [15] M. A. Aslam, S. Leitner, S. Tyagi, A. Provias, V. Tkachuk, E. Pavlica, M. Dienstleder, D. Knez, K. Watanabe, T. Taniguchi, D. Yan, Y. Shi, T. Knobloch, M. Waihl, U. Schwingenschlögl, T. Grasser, A. Matković, *Nano Letters* **2024**, *24*, 6529.